

A deep insight into a chemically homogeneous banded pumice sample: a role of crystal cargo immiscibility

LÜTFİYE AKIN

ERKAN AYDAR

ABDULLAH CEYLAN

A deep insight into a chemically homogeneous banded pumice sample: a role of crystal cargo immiscibility

Lütfiye AKIN^{1*}, Erkan AYDAR¹, Abdullah CEYLAN²

¹Department of Geological Engineering, Hacettepe University, Ankara, Türkiye

²Department of Physics Engineering, Hacettepe University, Ankara, Türkiye

Received: 15.06.2023 • Accepted/Published Online: 22.02.2024 • Final Version: 19.03.2024

Abstract: In this study, a set of representative banded rhyolitic pumice xenoliths collected from the ejecta of a basaltic cinder cone around Göllüdağ volcanic center, Central Anatolia, Türkiye, were characterized through whole-rock and mineral analyses, scanning electron microscopy (SEM), microcomputed tomography (μ -CT), and magnetization studies. The light- and dark-colored bands exhibit similar whole-rock chemistry, mainly distributed in rhyolite composition (71.35–71.66 wt.% SiO_2). The dark pumice band shows high crystallinity (12–14 vol.%) with abundant subhedral-euhedral phenocrystals, microphenocrystals, and microlites, and a glass composition consisting of 71–76 wt.% SiO_2 . In contrast, the light pumice band exhibits relatively low crystallinity (1.86–8.08 vol.%) with phenocrystals and/or microphenocrystals, and a slightly higher silica content (74–77 wt.% SiO_2). Both pumice bands display homogeneous distribution patterns with partially deformed and highly coalesced vesicles as observed through μ -CT and SEM studies. Additionally, we determined that the dark bands also contain magnetic minerals, which have a high attenuation coefficient and impart magnetic properties to the bands. The discrepancy in the crystal population between the light and dark pumice bands is attributed to the process occurring within the magma ascending throughout the conduit. We suggest that the response of the crystals involves separation and enrichment within their flow patterns, which prevents homogenization and results in a degree of mechanical immiscibility of the layers.

Key words: Banded pumice, computed tomography, vesicle size distribution, magnetic behavior, oxidation, immiscibility

1. Introduction

Banding in igneous rocks refers to a flow-related feature dependent on the preferential arrangement of the minerals (Smith, 2000). The alternating bands reflect either a complete physical and chemical mixture of two different magmas or a mingling of two magma compositions (Eichelberger et al., 2000; Coombs et al., 2000; Blundy and Cashman, 2008; Baker et al., 2012a; Andrews and Manga, 2014). The banding can also be formed by amygdaloidal precipitation of secondary minerals, welding of autobrecciated lavas, rheomorphic pyroclastic, or fragmentation during magma ascent (Gonnermann and Manga, 2005). Additionally, banded pumice is defined as a substantial product of erupted magma that records various eruption processes. The compositional banding of pumice is generally considered a result of mechanical magma mixing, referred to as “mingling” (Eichelberger, 1980; Koyaguchi, 1985, 1986; Bacon, 1986; Clynne, 1999; Waythomas et al., 2010).

The compositional and textural characteristics of banded pumice present pre-eruptive conditions of magma (Bardelli

et al., 2020; González-García et al., 2022). Textural studies of pumice have focused on vesicles and/or crystal size distributions to comprehend cooling histories, as well as the duration and style of eruption (e.g., Cashman and Mangan, 1994; Toramaru, 2014; Suhendro et al., 2022). Recent textural studies are primarily conducted through 2D and 3D image analyses. Numerous studies have demonstrated that X-ray computed tomography (CT) is a valuable technique due to its nondestructive characteristic, enabling the acquisition of high-resolution images at a micrometric scale for almost all types of materials. This technique has proven to be very suitable for overcoming the problems derived from 2D data, such as quantifying the spatial relationship of vesicles and determining their size distribution (Polacci et al., 2010; Voltolini et al., 2011; Baker et al., 2012b; Liedl et al., 2019). Previous studies have revealed the importance of CT in understanding the direct observations of the size, shape, and connectivity of vesicles, particularly for pyroclastic deposits with complex networks (Piochi et al., 2008; Voltolini et al., 2011; Baker et al., 2012a; Polacci et al., 2018).

* Correspondence: lutfiye_akin@hacettepe.edu.tr

In this study, we report qualitative and quantitative textural analyses of banded rhyolitic pumices found in basaltic cinder ejecta in the form of xenoliths. This study aims to reveal (i) the mechanism that causes the formation of the different bands and (ii) the petrologic relations among these bands by integrating complementary methods, including X-ray computed tomography, scanning electron microscopy, and magnetization measurements. Through the changes in magnetic properties along with textural, petrographic, and geochemical observations, we demonstrate that the observed heterogeneity in the color of banding is mainly caused by their crystal cargo. Consequently, we consider the immiscibility of crystal cargos and the oxidation of magnetic crystals, which favor the formation of dark band, as the possible mechanism of banding because it generates discrete thermomagnetic characteristics for each pumice band.

2. Materials and methods

2.1. Sample description and sampling strategy

The Göllüdağ volcanic complex is located south of the Cappadocia and belongs to the Central Anatolian Volcanic Province (CAVP; Toprak and Göncüoğlu, 1993). The CAVP was formed under a complex volcano-tectonic system between the Eurasian and Afro-Arabian plates during the Middle-Late Miocene (Figure 1a). The northward collisional movement of the Afro-Arabian plates caused the westward movement of the Anatolian block (Şengör and Yılmaz, 1981; Dirik and Göncüoğlu, 1996; Özsayın et al., 2013). During the Miocene–Holocene, volcanic activity occurred in Central Anatolia with numerous volcanic centers and volcanic products, resulting from the postcollisional extensional tectonic regime (Deniel et al., 1998; Dhont et al., 1998; Piper et al., 2002). The Neogene-Quaternary volcanism of Central Anatolia consists mainly of high-K calc-alkaline andesite-dacite, extensive rhyolitic and rhyodacitic ignimbrites of Cappadocia, and monogenetic volcanism, including maars, domes, and numerous scoria cones. The Erciyes Dağ and Hasandağ stratovolcanoes are composite volcanoes in the region and are situated on the Ecemiş and Tuzgözü strike-slip faults (Toprak, 1998). The Göllüdağ volcanic complex consists of silicic lava domes and associated basaltic cinder cones. The eruptive activity of Göllüdağ has been dated to the Middle Pleistocene (Bigazzi et al., 1997; Schmitt et al., 2011; Reid et al., 2017; Mouralis et al., 2019). This study focuses on a cinder cone, which is one of the Neogene-Quaternary monogenetic mafic volcanic products, occurring in bimodal association with rhyolitic volcanism scattered throughout the province (Innocenti et al., 1975; Le Pennec et al., 1994; Druitt et al., 1995; Reid et al., 2017; Dogan-Kulahci et al., 2018; Mouralis et al., 2019).

The products of the cinder cone mainly consist of red and black scoria, with occasional pumice xenoliths. The pumice clasts typically range from 1 to 15 cm in size. We sampled representative pumice clasts that contain significant banding within the cinder cone ejecta (Figure 1b). The pumice clasts have been identified as banded pumice, characterized by dark and light glassy bands separated by sharp contacts. The dark pumice bands partially contain bands of light pumice and exhibit heterogeneously distributed vesicles, along with euhedral-subhedral crystals. In contrast, the light bands are relatively crystal-poor and display a similar distribution of vesicle size to the dark bands (Figure 2).

2.2. Whole-rock chemical analysis

A band-concentrated pumice clast, with a size of 15 cm, was used for whole-rock chemical analysis. The light and dark bands of the banded pumice sample were cut from the parts with as much color homogeneity as possible. The cut parts of each band were subsequently pulverized using a ring mill in order to reach a grain size below 60 µm. Major element contents (Si, Al, Fe, Mn, Mg, Ca, Na, K, P, and Ti) were measured by Inductively Coupled Plasma-Optical Emission Spectrometry (ICP-OES) at ACME-Bureau Veritas Analytical Laboratories in Canada. The results are provided in Supplementary Table 1A.

2.3. Scanning electron microscopy (SEM)

We conducted chemical analyses of matrix glass (Supplementary Table 1B) and minerals (Supplementary Table 2) using a Carl-Zeiss EVO 50 EP scanning electron microscope (SEM) integrated with a Bruker AXS X-Flash 3001 silicon drift detector (SDD) electron dispersive X-ray spectrometer (EDS) at the laboratory of Hacettepe University, Department of Geological Engineering. Pumice samples were cleaned, prepared as thin sections, and carbon-coated before analysis. The SEM was operated with a 15 kV accelerating voltage at a 10 mm working distance. Beam currents ranging between 2 and 5 nA were set for both backscattered electron (BSE) imaging and EDS analyses. The spot diameter of the EDS spectra acquisition was 1–2 µm, and the counting time for characteristic X-ray intensities of selected elements (Na, Mg, Al, Si, K, Ca, Ti, Mn, and Fe) ranged between 90 and 120 s.

2.4. X-ray computed tomography (CT)

This study used the Bruker Skyscan 1272 microtomography device, installed at X-Ray Microtomography Laboratory of Hacettepe University Advanced Technologies Application and Research Center (HÜNİTEK). The data sets obtained from the scanning were transformed into 3D stacks using the InstaRecon reconstruction module. Sampling within the datasets, the thresholding, and other measurements were conducted using Bruker CTAn software. However, ImageJ software was used to determine the volume distribution of the mineral phases.

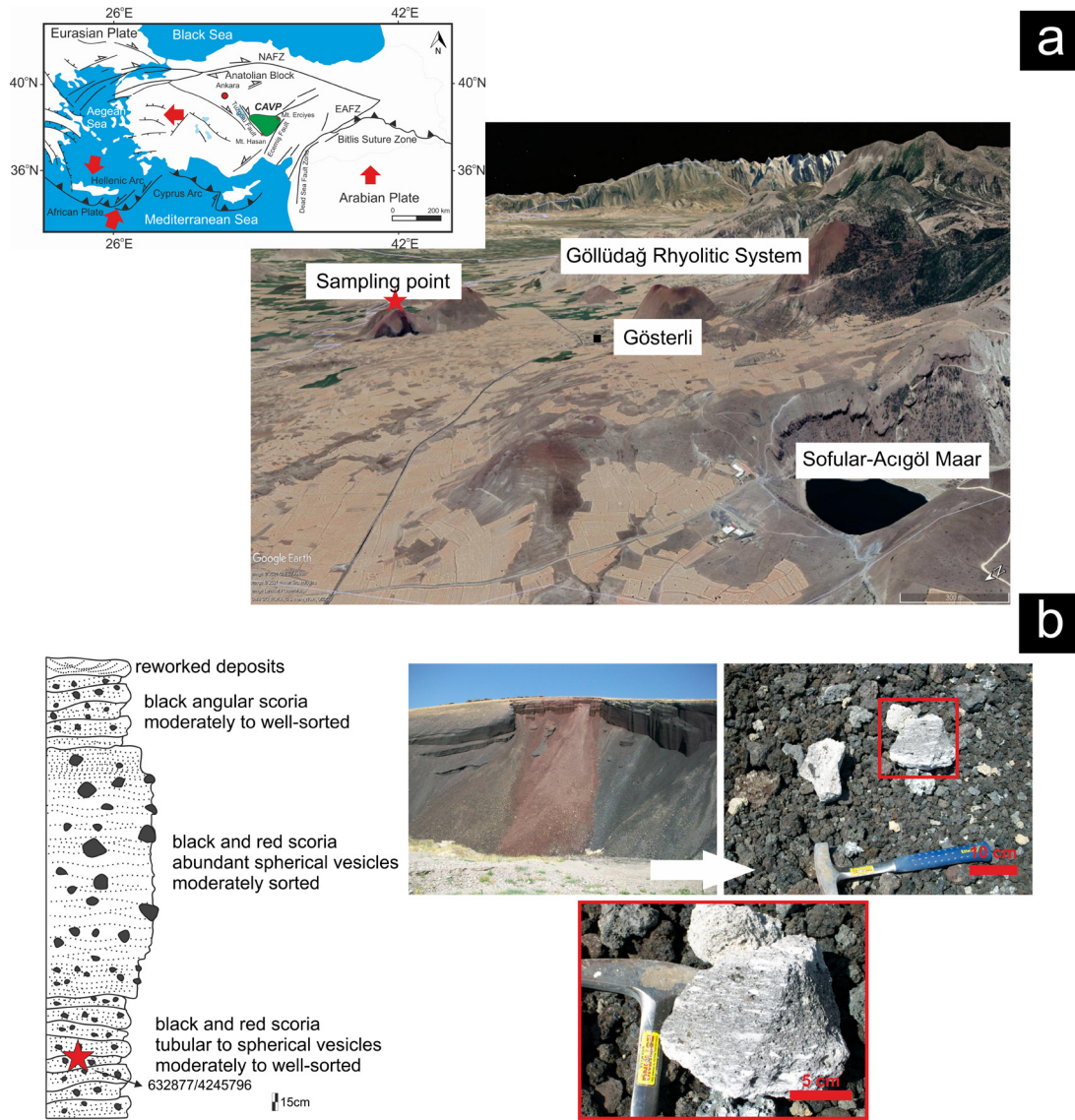


Figure 1. (a) The location of Gösterli-Göllüdağ Quaternary Bimodal Volcanism in Türkiye (Map data: Google Earth, CNES/Airbus image, 2021, Maxar Technologies, Landsat/Copernicus). The red star indicates the sampling site (CAVP: Central Anatolian Volcanic Province; NAFZ: North Anatolian Fault Zone; EAFZ: East Anatolian Fault Zone). (b) Composite stratigraphic column of cinder cone deposits showing the relationship between scoria and banded pumice clasts.

The banded pumice clast of 15 × 12 cm in size was selected for X-ray computed tomography application. The samples were prepared for the analysis by downsizing them to cylindrical forms with a diameter of 0.5 cm and a height of 1.3 cm from the original pumice clast (Figure 2). Subsequently, the pumice samples were scanned using 70 keV X-ray energy. These samples were placed on a stage, exposed to an X-ray beam, and rotated during the acquisition with rotation steps of 0.15° and 0.40°. The projections were recorded at regular steps over a total angular scan range of 360° and a random movement of 30°

to 40°. The X-ray projections were acquired as a stack of 2452 × 1640 pixels² gray-scale images. The samples were recorded in a white-beam configuration, filtering the X-ray beam with either 1 mm Al or 0.5 mm Al. Each image projection stack was treated similarly by reconstructing the set of 2D slices into 3D volume using CTAn software (Supplementary Figure). Reconstructed image stacks were then cropped out into a subvolumes. Visible noise in the dataset was frequently mitigated and softened by applying median and Gaussian blur filters. The despeckle filter was applied to remove nondescriptive small pixels. To extract

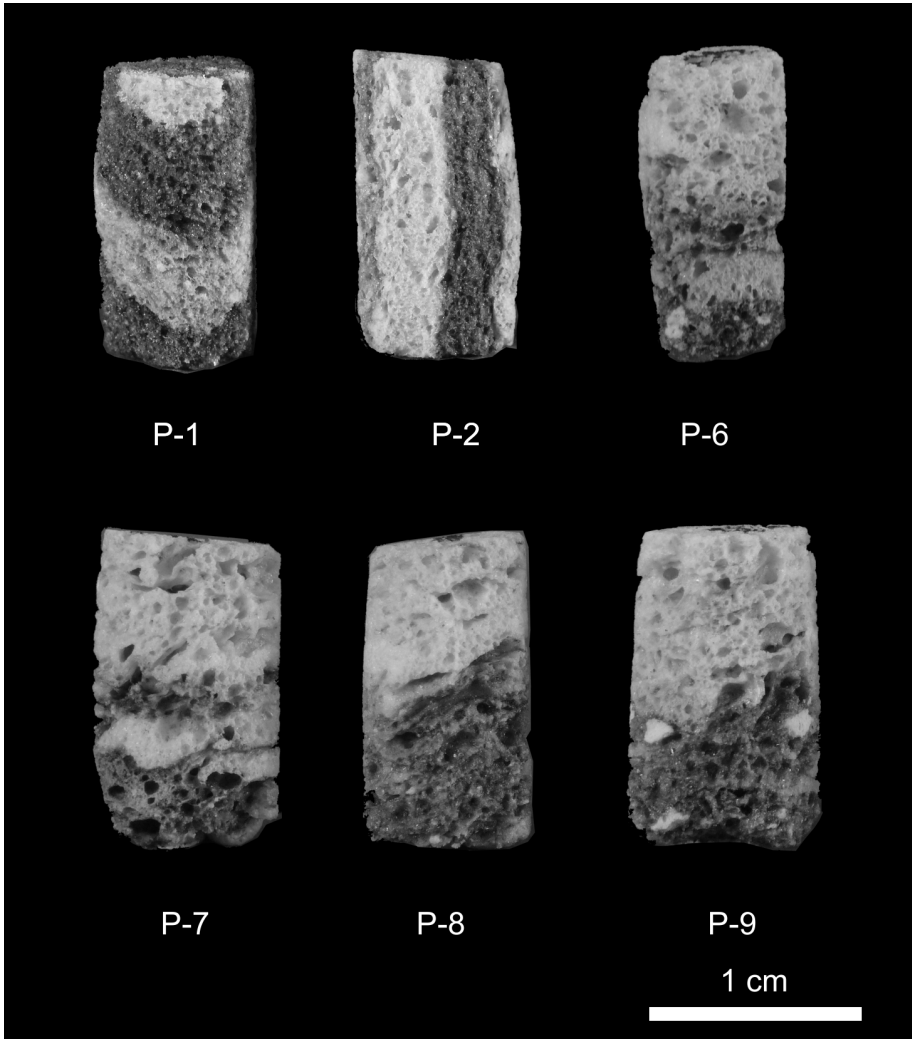


Figure 2. Photo images of cylindrical pumice samples for X-ray tomography application.

Table 1. Summary of mineral content and characteristics for the dark and light pumice bands obtained from SEM analysis.

Unit	Texture	Mineral content	Ø_{max} (μm)
Dark	• Crystal rich abundant porous hypohyaline porphyritic texture,	Pl	400
	• Subhedral-euhedral partially resolved feldspar,	Q	170
	• Subhedral-anhedral patchy-zoned orthopyroxene (Fe-rich in rim, Mg-rich in core) developed as cumulates,	Opx	150
	• Subhedral-anhedral partially rounded quartz,	Mag	
	• Magnetite is common as inclusion and phenocryst in ground mass, partially Ti exsolution	Py	
Light	• Porous, crystal-poor hypohyaline porphyritic texture,	Pl	500
	• Plagioclase is common as phenocryst,	Q	400
	• Partially rounded anhedral quartz crystals		

the volume of vesicles and visualize textural features from 3D representations, a volume of interest (VOI) was selected for each sample. We utilized a texturally representative volume ranging from 29.1 to 192 mm³, extracted from both bands, to rapidly obtain the data. Vesicles were segmented using manual gray-scale thresholding based on histogram values between 0 and 25 pixels of selected VOIs (Zandomenighi et al., 2010). Each slice of the samples was checked in different directions to avoid the presence of different phases, and threshold values for vesicles were selected for each sample. Pre- and postsegmentation correction filters were applied to prevent possible textural errors and refine the segmentation procedure. The unsharp mask was used to identify pixel values that differ from neighboring pixels in the gray-scale image. The pixel erosion was applied to dark pixels in the 3D dataset below the specified threshold value. Different mineral phases were distinguished based on the gray-scale intensity values. Segmentation was employed to identify mineral phases by thresholding specific ranges of the existing gray tones within the 3D dataset, subsequently forming a subdataset (Miller et al., 1990; Zandomenighi et al., 2010; Guntoro et al., 2019). The despeckle filter was then applied to remove nondescriptive pixels observed below a specific size in each band. Consequently, vesicle parameters and possible mineral assemblages were determined for both the dark and light bands of the pumice samples.

2.5. Magnetic properties

Room temperature magnetization measurements were conducted at the Hacettepe University Department of Physics Engineering laboratory. The samples were measured for susceptibility and hysteresis loops with backfield curves. Additionally, the acquisition of the magnetic properties was carried out using a physical properties measurement system (PPMS) by Quantum Design Inc. (San Diego, CA, USA). Samples used for magnetic measurements were prepared by ball-milling the pumice chunks to obtain microgranular powders. For room temperature hysteresis measurements, the powder-form samples were compressed onto a piece of Kapton tape, which was subsequently wrapped and inserted into a plastic straw tube for mounting on the sample holder. Conversely, high-temperature measurements were performed on powder samples embedded in a nonmagnetic, high-temperature cement, which was then applied to the sample holder.

3. Results

3.1. Major oxides

The major element concentrations of both glass and whole-rock are presented in Supplementary Table 1. The whole-rock geochemical composition of dark and light pumice bands shows no significant differences in

major element concentrations. Both bands have relatively similar values of SiO₂ (approximately 71 wt.%), Na₂O + K₂O (approximately 7.6 wt.%), and Fe₂O₃ (1.58 wt.%) for whole-rock compositions. The chemical analyses of dark and light pumice bands indicate rhyolite compositions with high SiO₂ contents (Figure 3a). The volcanic glass compositions of both dark and light pumice bands are mainly scattered within the subalkaline, high-potassium, and calc-alkaline volcanic rock associations. This group of volcanic products exhibits high SiO₂ (71–77 wt.%) and high K₂O (4.21–4.53 wt.%).

In this study, most of the analyzed glass compositions are peraluminous with a relatively high aluminum saturation index. In contrast, the whole-rock compositions are exclusively close to the metaluminous field (Figure 3b). The FeO and MgO contents are high in the dark bands but comparatively low in the light bands, both showing a significant decreasing trend with the increase of SiO₂ (Figures 3c and 3d). The volcanic glass of the dark bands exhibits FeO contents ranging from 1.13 to 2.43 wt.% (average value: 1.67 wt.%), while the light bands generally show FeO contents between 0.76 and 1.81 wt.% (average value: 1.2 wt.%). Additionally, MgO contents are ≤0.61 wt.% for dark bands (average value: 0.15 wt.%) and ≤0.07 wt.% for light bands (average value: 0.02 wt.%).

3.2. Pumice properties

The properties of pumice, including density and viscosity parameters for both dark and light bands, were calculated using the major oxide concentrations of the groundmass glass and whole-rock compositions (Figure 4). Density calculations were conducted using the DensityX program provided by Iacovino and Till (2019). The samples exhibit slight variations in melt density, ranging between 2.17 and 2.25 g cm⁻³ for dark bands (average value: 2.21 g cm⁻³), and between 2.17 and 2.23 g cm⁻³ for light bands (average value: 2.20 g cm⁻³). The average density values calculated from whole-rock compositions range from 2.25 (light band) to 2.28 g cm⁻³ (dark band) (Figures 4b and 4c). The results for both bands, based on whole-rock composition, demonstrate similar and higher density values compared to the glass. The higher densities observed in the dark and light bands overlap with those obtained from late-stage eruption products (Gualda, 2006; Gualda and Rivers, 2006). The viscosity of the groundmass glass in both dark and light bands was calculated using the equation proposed by Giordano et al. (2008). Values for each band were determined considering a range of crystallization temperatures (700–1200 °C) (Figure 4a). At crystallization temperatures ranging from 700 °C to 900 °C, the viscosity of the dark band changes from 4.57 to 6.54 Pa s, while the light band of the pumice exhibits higher values (between 4.73 and 6.72 Pa s) (Figures 4a and 4c).

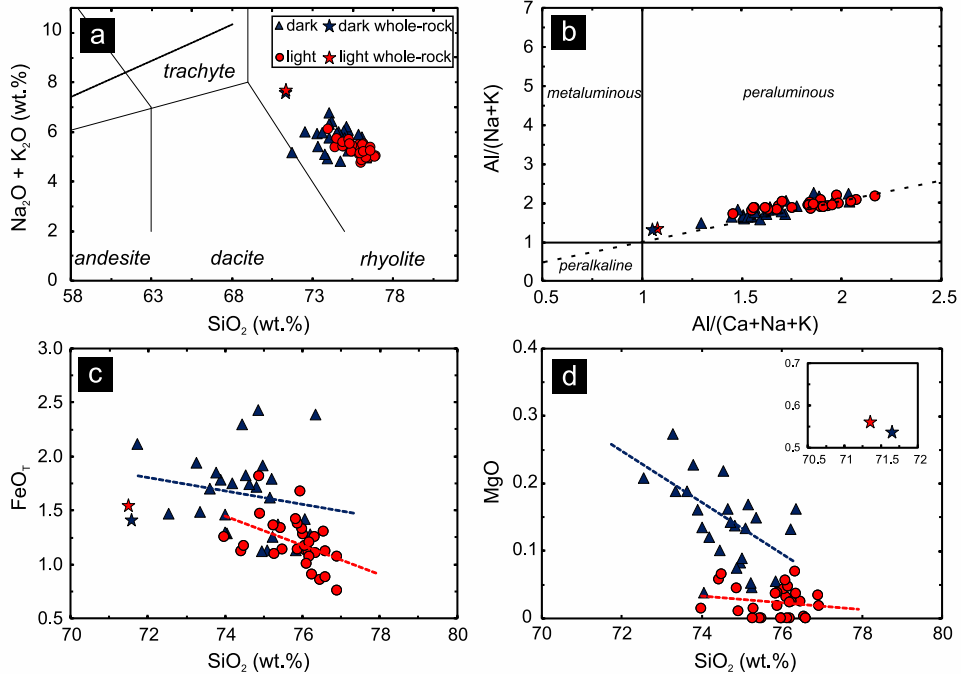


Figure 3. Geochemical characteristics for whole-rock and glass compositions of dark and light pumice bands. (a) Total alkali versus silica diagram (TAS; Le Bas et al., 1986); (b) aluminum saturation index (ASI) versus $Al_2O_3/Na_2O + K_2O$ (A/NK) diagram; SiO_2 versus FeO_T (c) and MgO diagram (d).

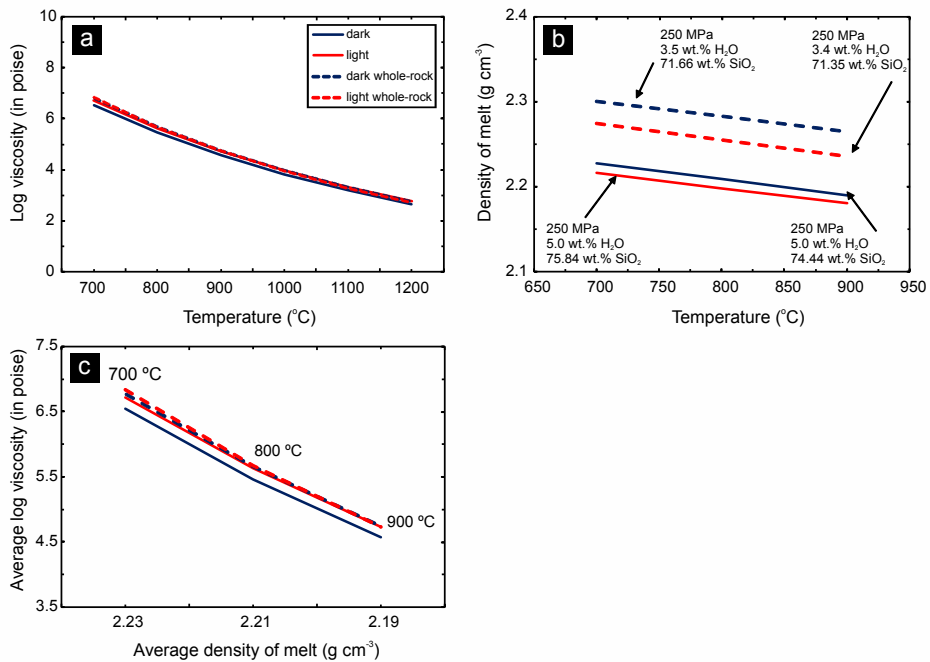


Figure 4. The diagrams of (a) log viscosity (in poise) and (b) melt density ($g\ cm^{-3}$) calculated from whole-rock and glass compositions at different temperature values. (c) The diagram of calculated density and viscosity values for rhyolitic glass and whole-rock compositions at temperatures between 700 and 900 °C.

3.3. Minerals

We identified four mineral phases: quartz, feldspar, pyroxene, and magnetite (+/- pyrite) (Supplementary Table 2). The mineral abundances indicate that most crystals are concentrated in the dark bands rather than the light ones. The light pumice bands only consist of feldspar and quartz, while the minerals of the dark pumice bands are feldspar, pyroxene, quartz, and magnetite (+/- pyrite) (Figures 5 and 6).

The feldspar association comprises plagioclase ranging from oligoclase to labradorite composition (An_{20-70} , An_{24-63}), with subordinate alkali-feldspar (sanidine) present in both bands (Figure 7a). The plagioclase phenocrysts range from 250 to 500 μm in size. Within the dark pumice bands, these crystals are relatively smaller, measuring between 280 and 385 μm . Generally, the plagioclase phenocrysts exhibit a normally zoned core and overgrowth rims with oscillatory zoning. Microphenocrysts of plagioclase typically range from 100 to 170 μm in size. Plagioclase microlites are euhedral, and their size ranges between 70 and 80 μm (Noguchi et al., 2008; Suhendro et al., 2022; Bernard et al., 2022). Pyroxenes are less abundant than plagioclase and indicate an orthopyroxene composition. These are represented by euhedral enstatite (En_{60-90} , Fs_{10-40} , Wo_{0-5}) microcrystals scattered in the glassy matrix (Figures 5b and 7b). Orthopyroxene crystal sizes range between 18 and 25 μm , with some reaching up to 150 μm . Anhedral pyroxenes are predominantly found as cumulates with plagioclase and/or other pyroxenes. Pyroxenes exhibit patchy zoning, with almost all having Fe- and Al-rich rims. Quartz crystals are typically anhedral and commonly fragmented or rounded (Figures 6b and 6d). Their sizes range between 70 and 142 μm in the dark bands and extend up to 400 μm in the light bands of pumice (Table 1). Magnetite is commonly found in the dark bands of pumice. It is typically under micron size but occasionally reaches sizes of up to 150 μm (Figure 5c). Pyrites are typically euhedral, measuring less than 10 μm , and are commonly found in dark pumice bands (Figure 5d).

3.4. Identification and distribution of minerals

We used threshold values to accurately identify minerals and/or mineral groups from computed tomography image data. However, this procedure was difficult because multiple filtering could only partially remove the noise generated during the acquisition. Grain classification substantially depends on contrast values derived from X-ray attenuation differences between mineral phases (Miller et al., 1990). According to this, the main mineral phases identified include plagioclase, quartz, orthopyroxene, and magnetite (+/- pyrite), as presented in the petrological study. Due to their high adsorbing nature, the presence of Fe-Ti oxides (+/- pyrite) could be easily determined. Notably, there is a significant contrast between magnetite (+/- pyrite), orthopyroxene, and tectosilicates, whereas plagioclase and quartz exhibit no significant difference (Figure 8).

The pyroxenes exhibit relatively high gray levels, whereas feldspar (plagioclase) and quartz show gray levels similar to that of the matrix glass. Consequently, distinguishing between these phases based solely on color is nearly impossible (Miller et al., 1990; Guntoro et al., 2019). However, they can be differentiated from the glass by their crystal shapes. The vesicles can be identified as dark spaces with no adsorbent behavior (Zandomenighi et al., 2010) (Figure 8). The reliability of this classification may be subject to debate, particularly when applied to tiny crystals. The main reason for the difficulty in identifying tiny crystals is that raw data already contains noise. Consequently, the light parts of the analyzed volume of pumice display lower crystal content compared to the dark pumice bands (Table 2). The volume percentages of minerals, calculated from representative banded pumice, indicate that light pumice bands contain approximately 1.86–8.08 vol.% crystals, whereas the light pumice bands mainly comprise feldspar and quartz crystals with 1.19–7.52 vol.%. While pyroxene and Fe-Ti oxide are not observed in petrographic studies, the thresholding process of 3D tomography images revealed the presence of relatively small-sized crystals in the light pumice bands

Table 2. Representative crystal content of dark and light pumice bands calculated from 3D-constructed volumes using ImageJ software.

Sample		Crystal content (vol.%)				
		Fld+Q	Prx	Mag+Py	Glass	Vesicles
P-6	Dark	8.16	3.04	0.17	28.54	60.09
	Light	1.19	0.50	0.17	32.58	65.56
P-7	Dark	10.13	0.87	0.20	30.33	58.47
	Light	5.90	0.56	0.09	36.96	56.49
P-8	Dark	10.24	1.20	0.74	45.02	42.80
	Light	7.52	0.33	0.23	54.58	37.34
P-9	Dark	8.34	2.52	0.16	42.98	46.00
	Light	7.10	0.08	0.05	43.62	49.15

Fld: feldspar; Q: quartz; Prx: pyroxene; Mag: magnetite; Py: pyrite.

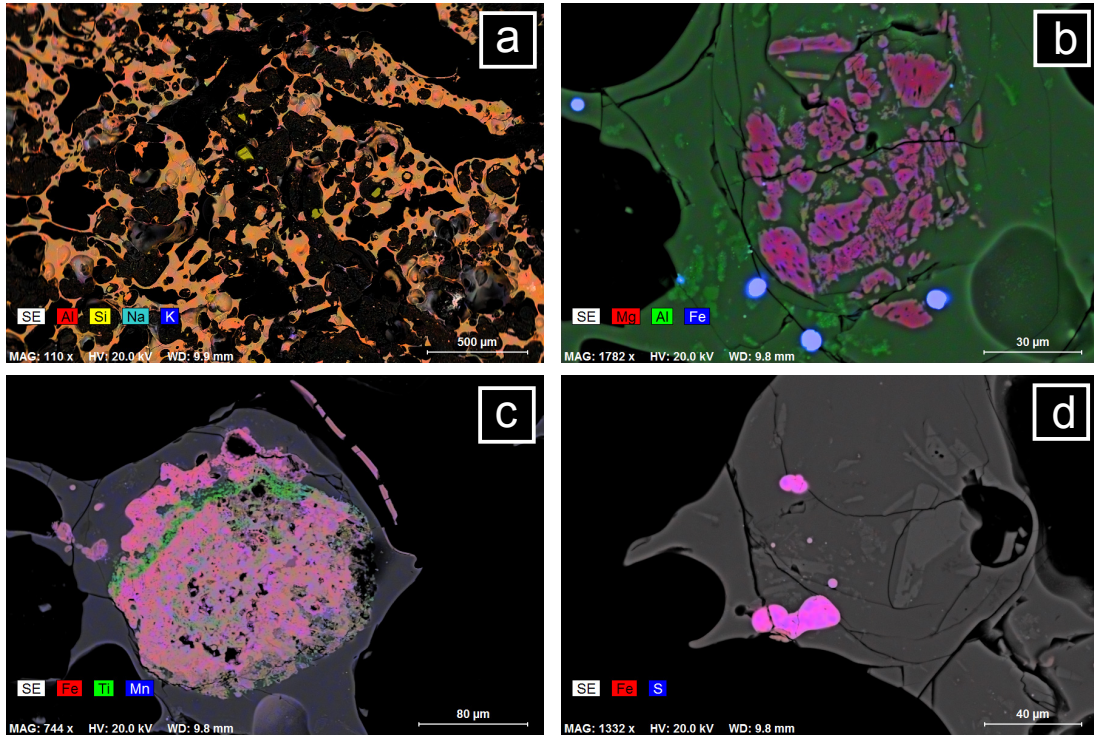


Figure 5. Scanning electron microscope EDS elemental map for minerals in the dark band of the pumice sample. (a) Volcanic glass and vesicles; (b) pyroxenes; (c) magnetite with Ti exsolutions; (d) pyrite crystals scattered in a glassy matrix.

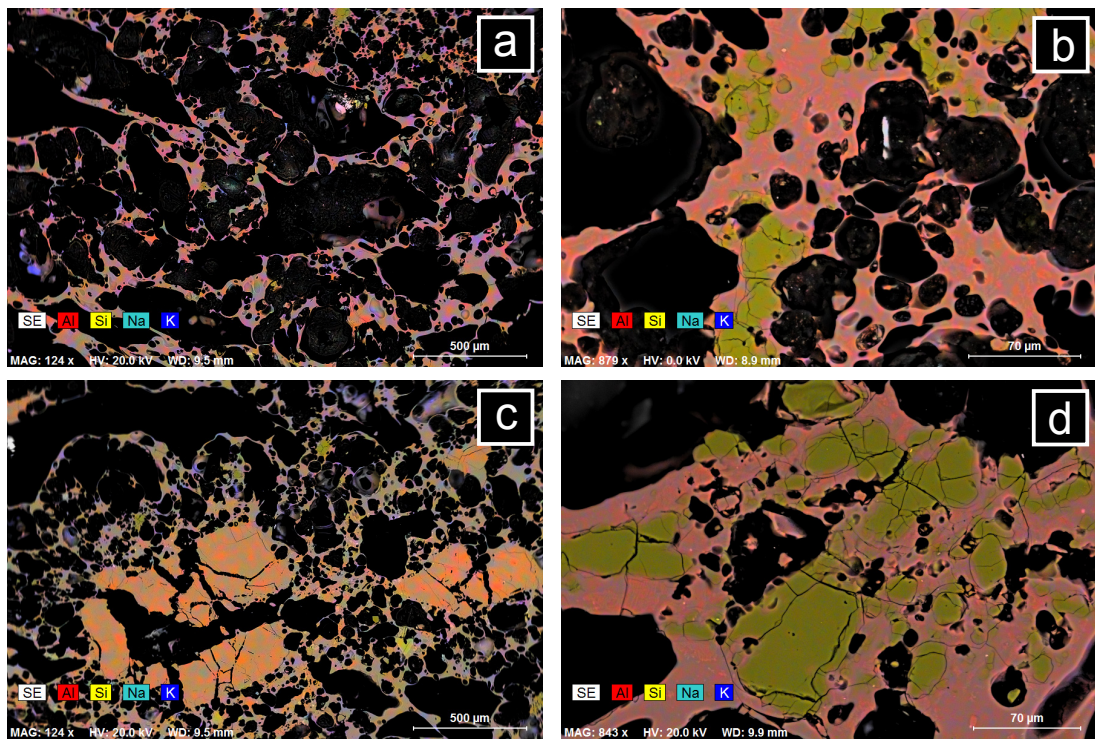


Figure 6. Scanning electron microscope EDS elemental map for minerals in the light band of the pumice sample. (a) Volcanic glass and vesicles; (b and d) anhedral quartz crystals; (c) plagioclase.

(0.08–0.50 vol.%). Dark pumice bands exhibit a higher crystal content, nearly 12 vol.%, consisting mainly of feldspar, quartz (8.16–10.13 vol.%), and pyroxenes (0.87–3.04 vol.%). Additionally, Fe-Ti oxides display different abundances in dark (0.74 vol.%) and light (0.23 vol.%) bands, respectively (Table 2).

3.5. Vesicles

The application of X-ray tomography yields crucial parameters for high-resolution analysis of vesiculation in volcanic rocks. Additionally, it aids in quantifying the internal structure and texture of the volcanic products through 3D visualization of boundary relations among crystals, matrix,

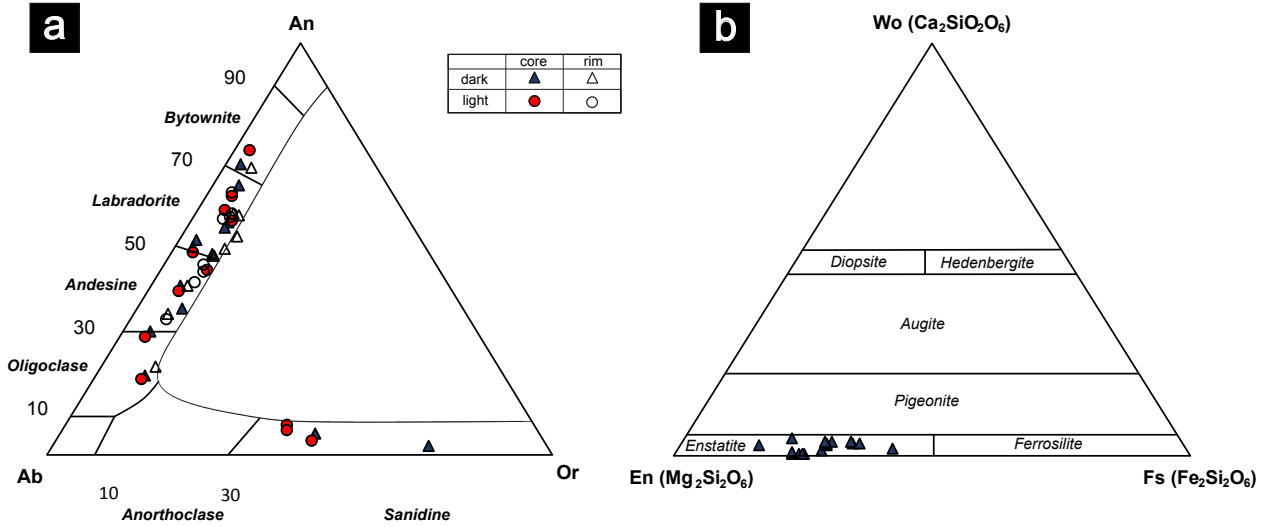


Figure 7. Mineral classification diagrams of plagioclase (a) and pyroxene (b) for the dark and light bands from banded pumice clast.

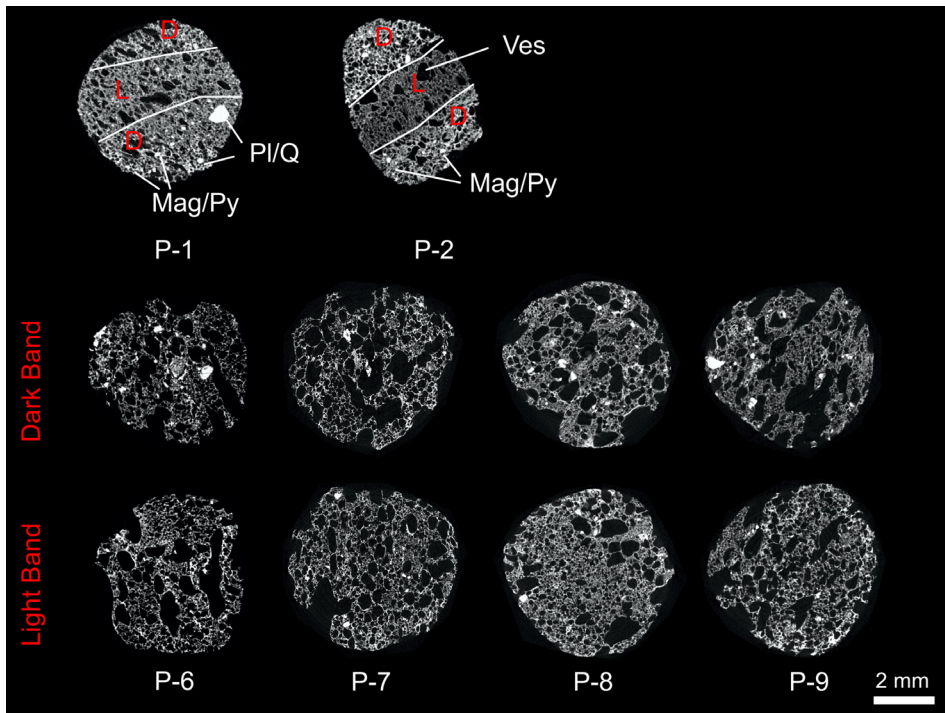


Figure 8. Original reconstructed 2D image slices of dark and light pumice bands, with possible mineral assemblages (Mag: magnetite, Py: pyrite; Pl: plagioclase; Q: quartz; Ves: vesicle).

and vesicles. This study shows that pumice samples exhibit porosities ranging from 31 to 66 vol.%, calculated from segmented voxel volumes. The interconnectivity of vesicle within the selected volume indicates that most pumice vesicles are interconnected, with relatively coherent values between 87.49 and 100 vol.%. However, the resolution of the method might also limit the observation of very thin vesicles, and a small fraction of the vesicle appears to be isolated and generated as closed pores within the analyzed VOIs. Textural observation of pumice samples and 3D constructed volumes reveals that the isolated vesicle represents a negligible component (0.0012–3.43%) of the total volume.

The individual vesicles within the analyzed volumes are predominantly spherical to elongated in shape. The 3D reconstructed volumes of pumice indicate that the circularity of the samples is between 0.70 and 0.80, while the average eccentricity ranges from 0.53 to 0.68. These findings signify a notable variation in vesicle shapes,

transitioning from circular to elliptical forms (Table 3). Through 3D observations, four groups of vesicles can be distinguished based on size: <150 μm (small), 150–350 μm (medium-1), 350–550 μm (medium-2), and >550 μm (large). The volume percentage (n) of vesicles varies widely within each group, with $n_{large} \leq n_{medium-2} < n_{medium-1} \leq n_{small}$. However, the abundance of vesicles within each group varies among samples and between the dark and light bands of individual pumice sample. The calculated open pore volume ranges from 30.03 to 65.50%. All samples exhibit a right-skewed distribution of vesicle sizes, with the mode at 150 μm (Figure 9). The tails of the vesicle size distributions indicate either an increase or decrease in vesicle size over a given diameter range. In our study, vesicles dominantly develop with a pore diameter ranging between 10 and 350 μm. The vesicle size distribution (VSD) of these samples is highly polydisperse and bimodal, likely reflecting multiple minor modes of the size distribution (Figure 9).

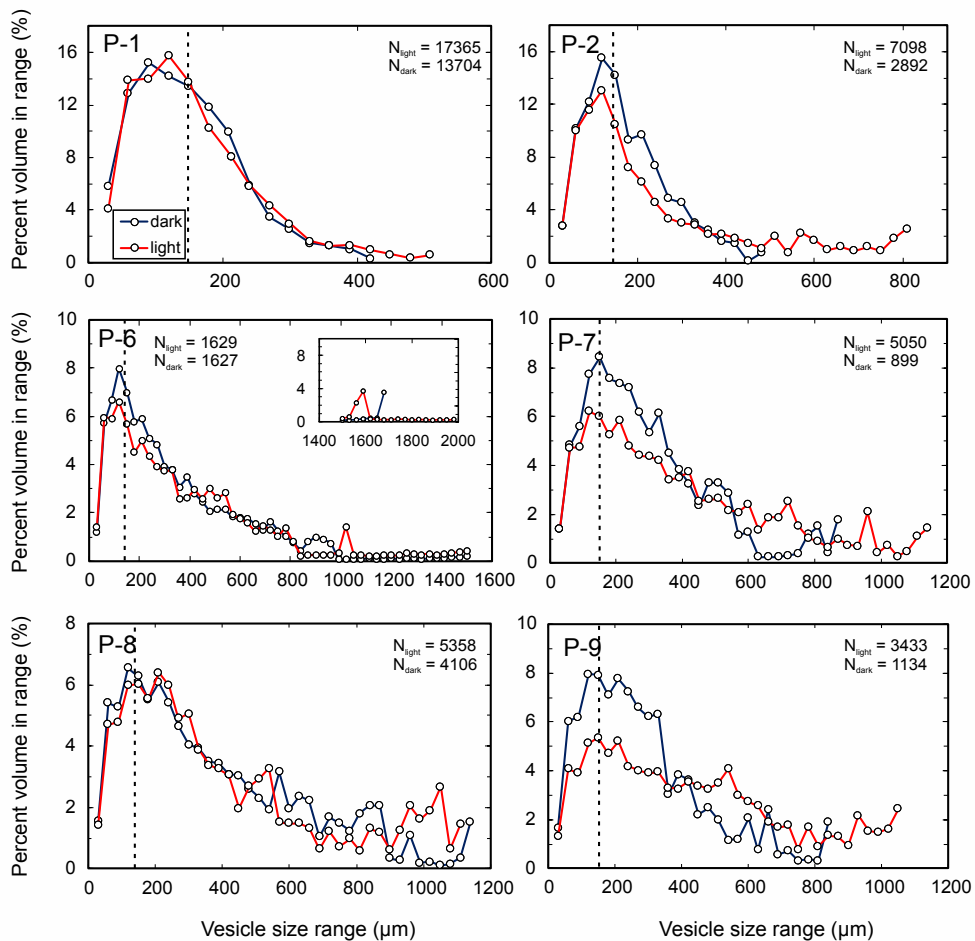


Figure 9. The 3D vesicle size distributions (VSDs) of the pumice samples analyzed by X-ray CT. The size distributions are presented as the percentage volume in range versus vesicle size range (μm). N indicates the number of particles analyzed, and the dotted line shows the main peak level of 150 μm.

Table 3. Three-dimensional vesicle parameters of dark and light pumice bands, calculated with CTAn software.

Sample	P-1		P-2		P-6		P-7		P-8		P-9	
	Dark	Light	Dark	Light	Dark	Light	Dark	Light	Dark	Light	Dark	Light
Total volume (VOI)	4.83×10^{10}	1.09×10^{11}	2.91×10^{10}	4.67×10^{10}	1.38×10^{11}	1.13×10^{11}	3.96×10^{10}	1.92×10^{11}	1.28×10^{11}	1.34×10^{11}	4.28×10^{10}	1.04×10^{11}
Porosity (pore volume)	%	22.32	30.79	46.28	60.09	65.56	58.47	56.49	42.80	37.34	46.00	49.15
Open pore volume	%	34.92	19.24	30.03	46.18	60.03	65.50	58.35	41.96	34.52	45.68	48.53
Closed pore volume	%	0.56	3.81	0.77	0.19	0.15	0.18	0.28	1.44	4.32	0.61	1.22
Average circularity		0.80	0.75	0.74	0.75	0.80	0.78	0.86	0.81	0.81	0.82	0.82
Average eccentricity		0.62	0.67	0.67	0.68	0.62	0.65	0.55	0.63	0.62	0.61	0.61
Roundness		0.63	0.59	0.60	0.60	0.63	0.61	0.70	0.63	0.64	0.65	0.65
Vesicle number density	mm^{-3}	2.83×10^2	1.59×10^2	1.0×10^2	1.52×10^2	0.12×10^2	0.15×10^2	0.23×10^2	0.30×10^2	0.40×10^2	0.27×10^2	0.33×10^2
Average pore surface density	$\frac{\text{mm}^2}{\text{mm}^3}$	1.24×10^{-2}	8.16×10^{-3}	1.02×10^{-2}	1.30×10^{-2}	1.09×10^{-2}	9.89×10^{-3}	1.20×10^{-2}	1.01×10^{-2}	8.28×10^{-3}	7.03×10^{-3}	8.17×10^{-3}
Total volume of pore space	μm^3	1.71×10^{10}	2.43×10^{10}	8.96×10^9	2.16×10^{10}	7.38×10^{10}	8.30×10^{10}	2.32×10^{10}	1.09×10^{11}	5.49×10^{10}	1.95×10^{10}	5.13×10^{10}

3.6. Magnetization measurements

The hysteresis loop and its backfield curve plot present the induced magnetization of the sample in response to an applied magnetic field. Hysteresis data were obtained for both dark and light bands of the pumice sample, including room-temperature and high-temperature measurements. Figure 10 presents the room temperature hysteresis (a, c) and thermomagnetic curves (b, d) recorded under an applied magnetic field of 20 kOe. Room temperature hysteresis curves exhibit a typical ferrimagnetic behavior of core-shell structured nanoscaled magnetite particles, characterized by a magnetite core surrounded by a nonstoichiometric FeOx shell. This could be attributed to the rapid condensation of pumice samples following the cooling of the volcanic fragments, resulting in the formation of nanoscaled magnetite regions. The nature of these magnetic components reflects themselves as high local magnetic anisotropy, impeding complete magnetic saturation even at 20 kOe. The light band is determined to have a coercivity of approximately 425 Oe, which is larger than the coercivity of the dark band by approximately 200 Oe. These values are also comparable to those reported for multidomain magnetite nanoparticles (Li et al., 2017). The limit distinguishing between single and multidomain sizes for magnetite falls within the range of 76–128 nm (Butler and Banerjee, 1975; Leslie-Pelecky and Rieke, 1996). Therefore, the average size of magnetite particles in light and dark bands of pumice samples is expected to fall in this range. The relatively higher coercivity observed in the light band can be attributed to the significant substitution relationship between the core and the nonstoichiometric shell of the magnetite nanoparticles within the light band.

Thermomagnetic measurements also reveal significantly different magnetic behaviors for both bands. While the dark band exhibited a predominant, relatively sharp reduction of the magnetization around 275 °C, the light band experienced a gradual reduction of the magnetization starting around 425 °C. The differences in transition temperatures stem from the size dependence of the Curie temperature for the noninteracting embedded magnetite nanoparticles (Ling-fei et al., 2007). It is known that the Curie temperature decreases with a decrease in particle size (Butler, 1998; Piper et al., 2002; Ozima et al., 2003). Therefore, the core size of the magnetite nanoparticles for the dark band is smaller than that of the light band. Furthermore, during the cooling cycle, both samples experience an increase in magnetization below approximately 250 °C, resulting from the same type of magnetic ordering. This is attributed to a temperature-induced rearrangement and/or to the oxidation of the samples' nonstoichiometric FeOx shell, leading to a higher magnetization at room temperature. This effect appears to be more significant for the dark bands, indicating that

magnetite nanoparticles acquire larger disordered shells around the core. Based on these observations obtained through magnetization measurements, one can develop a model for the magnetite nanoparticles within the light and dark bands of the pumice samples, as depicted in the insets of Figures 10b and 10d.

4. Discussion

4.1. The formation of the vesicle populations

Vesicles provide valuable information about the ascent conditions for the erupted magma volume. The textural variation of eruptive products is related to the size and shape of vesicles, which, in turn, may be modified after fragmentation due to the growth of bubbles and/or stretching during transportation within the conduit (Cashman and Mangan, 1994; Gualda and Rivers, 2006; Gualda, 2006; Shea et al., 2010). Small- and medium-sized vesicles typically represent the initial stage of the vesiculation process. They are usually formed in the conduit during magma ascent due to high degrees of supersaturation. The variation in vesicle size within the groundmass suggests second-generation vesiculation, primarily containing small and medium-sized vesicles that later developed into other vesicles of similar sizes. However, relatively large vesicles can be produced by coalescence and postfragmentation expansion (Gurioli et al., 2008; Shea et al., 2010; Toramaru, 2014; Suhendro et al., 2022).

The dark and light bands of the analyzed pumice samples exhibit relatively high porosity, with most vesicles displaying textural evidence indicative of interaction and coalescence (Figure 11). The primary parameter characterizing vesicle shape in volcanic products is roundness, with values ranging from 0.59 to 0.70 for both light and dark pumice bands. Bulk vesicles, reaching sizes of up to 3 mm, demonstrate a deformed to partially deformed character. Subrounded shapes are common in both light and dark pumice bands (Figures 2 and 8). Both light and dark bands contain heterogeneous and coalesced populations of vesicle within a glassy groundmass (Figures 6c and 6d). The elongated vesicles often exhibit tubular forms and are associated with nondeformed, spherical small vesicles (<5 µm) (Figures 5a and 6b). Homogeneous, less deformed, and poorly coalesced vesicles are also common in the glassy groundmass of light and dark pumice bands (approximately 35 µm). The walls between these vesicles are partially broken and/or have unresolved thin structures. The vesicle walls in the light and dark pumice bands are mostly similar, with a thickness of 10 µm (Figures 5a and 6a).

Vesicles in volcanic rocks undergo vesicle collapse during the open system degassing, resulting in the formation of various vesicle shapes, including large,

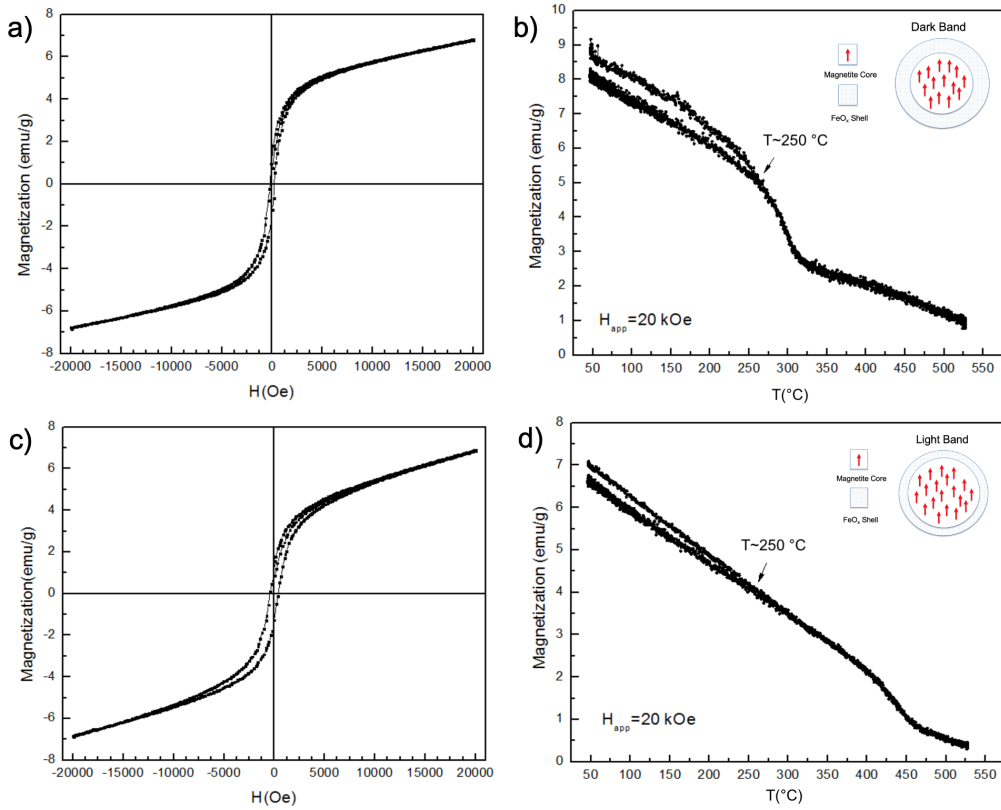


Figure 10. Room-temperature hysteresis (a, c) and thermomagnetic magnetization (b, d) curves of dark and light pumice bands, respectively.

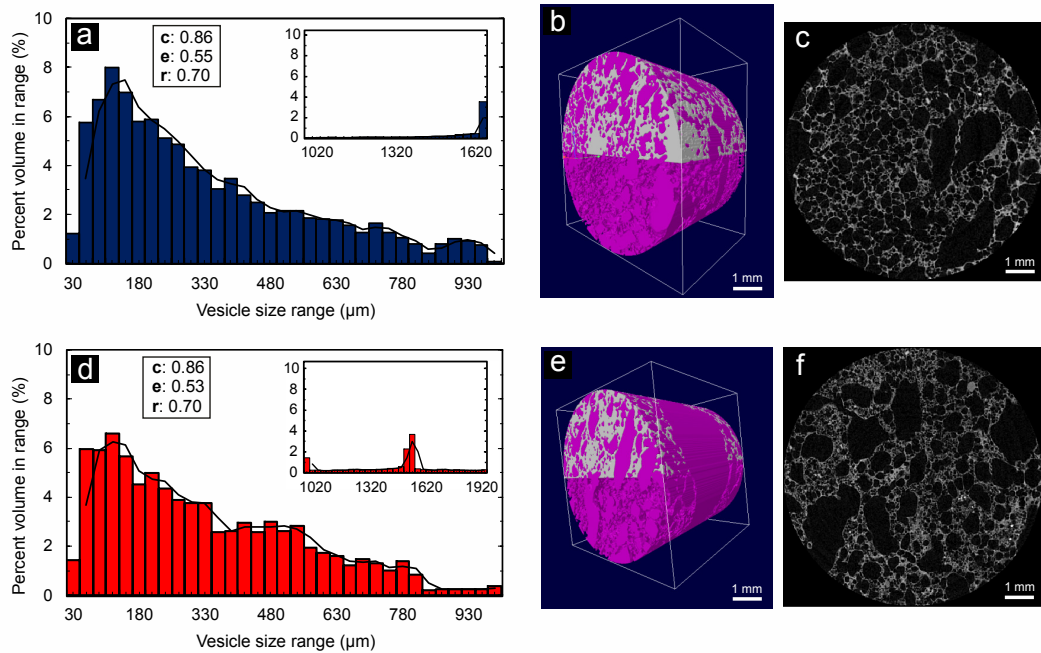


Figure 11. The size distribution histograms of vesicles from a selected sample (a: dark band; b: light band) (c: circularity; e: eccentricity; r: roundness). The 3D-constructed model of vesicles for dark (b) and light (e) pumice bands, and 2D slices from the 3D volume of dark (c) and light (f) pumice bands.

elongated, and more complex forms ranging in size from microns to centimeters (Klug et al., 2002; Wright et al., 2009; Moitra et al., 2013). The size distributions are mostly irregular due to various modes and sharp transitions between VSD patterns. The vesicle population within both bands of pumice clasts is typically characterized by several significant populations. Small-sized vesicles, measuring less than 150 μm , are mostly spherical in shape, whereas medium-sized vesicles exhibit two size ranges: 150–350 μm and 350–550 μm , both indicating a syneruptive origin. Large vesicle populations display a size range of 550–750 μm , mostly occurring as a combination of small and medium-sized vesicle populations. The large vesicles may also form either during crystallization or after the fragmentation of phenocrystal phases. The large, nonuniform, and channel-like vesicles are also observed in both pumice bands, likely formed in the conduit before eruption (Giachetti et al., 2011; Berg et al., 2016). In this study, the abundance of small vesicles suggests secondary nucleation, while the presence of large vesicles indicates vesicle coalescence. The combination of these processes in the pumice clast may explain the similar rates of variation observed in the size distribution of vesicle populations (Toramaru, 2014; Suhendro et al., 2022).

4.2. The origin of magnetite and the crystal fragmentation
The computed tomography results were compared to the data obtained from the petrographic observations. They provided similar information on vesiculation characteristics and mineral assemblages. The two procedures are especially well-agreed upon qualitatively and quantitatively regarding the oxide distribution in both pumice bands (Figure 12). Despite silicates being more abundant than magnetite crystals, one of the most crucial textural pieces of evidence obtained from 2D and 3D images is that magnetite crystals are primarily scattered in the dark pumice band (Figure 12). Furthermore, Fe-Ti oxides are commonly considered to crystallize at the nucleation sites of vesicles in silicate melts due to their differing chemical and structural properties. Under magmatic conditions, the crystallization of magnetite reduces surface tension, thereby enabling more effective attachment of magnetite to the melt compared to silicate minerals (Gualda and Ghiorso, 2007; Gualda and Anderson, 2007). However, the crystallization of silicate minerals, such as feldspar and quartz, is required to obtain a significant amount of magnetite crystals, and there exists supporting evidence for this.

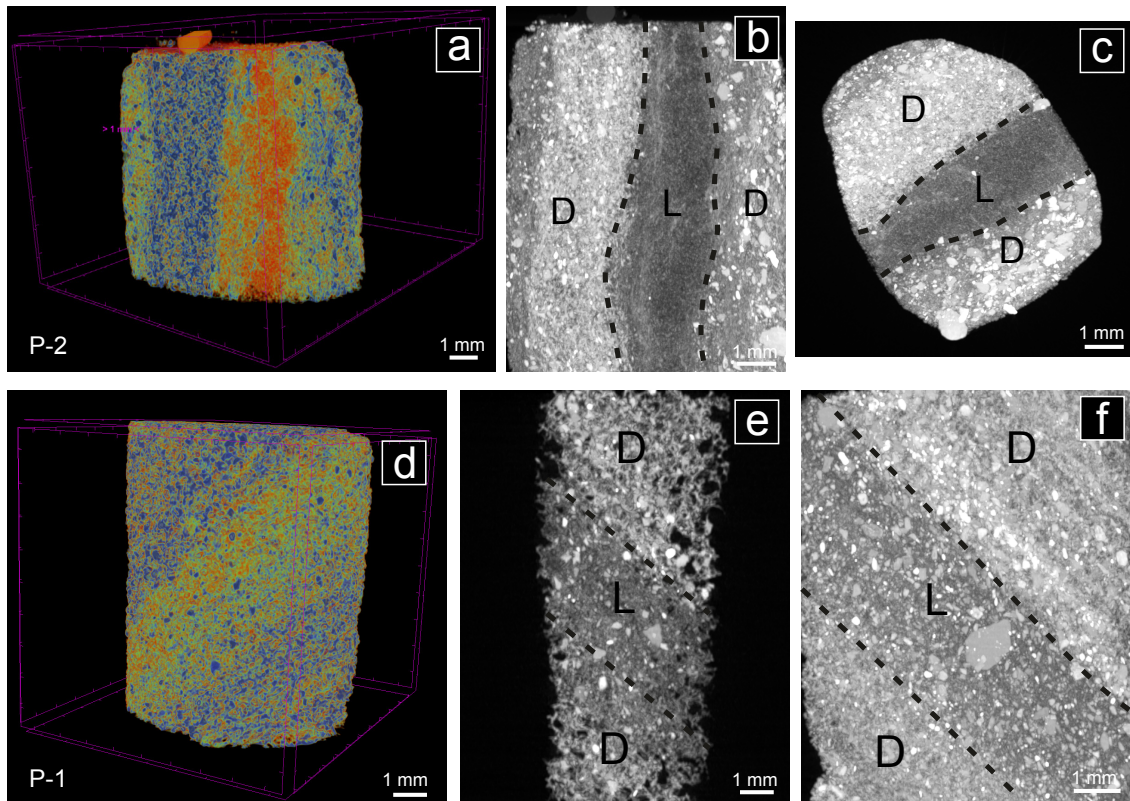


Figure 12. The 3D-constructed volume of P-1 (d) and P-2 (a) banded pumice samples. Horizontal (c and f) and vertical cross sections of (b and e) 3D-constructed volumes. The variations in gray-scale intensity suggest the presence of both dark (D) and light (L) bands, as well as different mineral phases within the pumice clast.

Moreover, the vesicle formation causing local oxidation of the original melt may also initiate magnetite crystallization (Candela, 1986; Gualda and Ghiorso, 2007). Additionally, to crystallize 1 mg of magnetite, approximately 0.72 mg of Fe would be necessary (Gualda, 2006; Gualda and Anderson, 2007). The residual melt of the early erupted products contains 0.76–1.81 wt.% and 1.13–2.43 wt.% FeO in light and dark pumice bands, respectively, thereby supporting the concept of oxidation in melt and magnetite crystallization.

The size and abundance of crystals can provide important information about the crystallization history of igneous rock (Cashman, 2020). However, such textural studies of pyroclastic products are more difficult due to the high porosity and low crystal content of the rock (Marsh, 2007; Hersum and Marsh, 2007; Baker et al., 2012b). In the studied samples, the crystals are generally isolated compared to plutonic rocks, and they occur mainly as scattered phases within a vesiculated glassy matrix. In both bands of the examined pumice sample, several fragmented crystals are observed. Phenocrystal fragments larger than 400 μm typically exhibit irregular shapes with cracks and lack a glass coating. There is no later-stage melt filling observed between the fragmented crystals, and some crystals are found to be associated with the generation of large vesicles. Quartz crystals are also fragmented and predominantly occur as rounded fragments that are fully coated by a glassy matrix. These fragments exhibit evidence of early crystallization by being absorbed into the melt with wet surfaces (Gualda et al., 2004; Gualda and Anderson, 2007). The sizes of feldspar and quartz are similar in light pumice bands but different in dark ones. This observation may indicate a similar fragmentation history for feldspar and quartz in light pumice bands, contrasting with the dark ones (Gualda and Rivers, 2006; Gualda and Anderson, 2007; Gualda and Ghiorso, 2007). Quartz and feldspar fragmentation predominantly signify the outcomes of different processes that occurred during both the preruptive and syneruptive/deposition stages at the time of magma ascent (Cashman and Mangan, 1994).

4.3. Compositional variation of pumice bands

Light and dark pumice bands have similar compositions despite showing different crystal contents and magnetization behaviors. Both types of bands display rhyolitic whole-rock chemistry, with very identical SiO_2 content (approximately 71 wt.%). The matrix glass of both the dark and light pumice bands predominantly consists of rhyolite, covering a compositional range between 71 and 77 wt.% SiO_2 , while the mineral assemblage in each band exhibits significant differences. Furthermore, the similarity in the $\text{K}_2\text{O}/\text{Na}_2\text{O}$ ratios (1.32, 3.96, and 1.32, 3.94 for light whole-rock, light band matrix glass, and dark whole-rock, dark band matrix glass, respectively) suggests formation

from a compositionally similar source. The differences in petrography and magnetization observed between light and dark pumice bands are not directly related to the chemical conditions in the preruptive magma, but rather to changes in the physical properties of the magma during the eruption (Polacci et al., 2001; Rosi et al., 2004).

Experiments on crystallization kinetics have demonstrated that the cooling rate influences the size, shape, and the rate of crystallization of crystals (Couch et al., 2003; Piochi et al., 2008). Dark pumice bands typically include rhyolitic matrix glass and significant crystals of plagioclase and mafic minerals. The viscosity value may vary due to the differences in phenocryst and microlite contents. The nearly identical viscosity values for both light band glass matrix and their whole-rock compositions between 900 and 950 °C show that crystal content has minimal influence on viscosity (Figures 4a and 4c) (Piochi et al., 2008; Whittington et al., 2009). However, the relationship between viscosity and crystal content indicates a 3-fold increase in viscosity for crystallinity levels between 20 and 25%, and a 15-fold increase for crystallinity levels above 40% (Spera, 2000; Whittington et al., 2009). Temperature and water contents can have a much more significant effect on viscosity than crystallinity, at least at low crystallization rates (4.5% and 13% for light and dark pumice bands, respectively). If the temperature change has only a modest effect on liquid viscosity, even small changes in water content cause significant variations in viscosity in a rhyolitic melt. For example, increasing the water content from 1 to 5 wt.% results in a decrease in viscosity from 7.94 to 5.47 Pa s at 850 °C (Polacci et al., 2004; Whittington et al., 2009). A large density difference and a low viscosity (favored by a high-water content) are required for an efficient crystal-melt separation (2.28 and 2.25 density values, and 3.5 and 3.4 wt.% water content for dark and light whole-rock, respectively). The low melt viscosity also favors convective mixing and crystal segregation (Piochi et al., 2008; Whittington et al., 2009). As a result, light and dark pumice bands may have experienced different rheological histories during formation, even though they share nearly identical composition and texture, reflecting variations in temperature, crystallinity, and water content during the evolution of the residual melt (Polacci et al., 2001; Rosi et al., 2004; Gurioli et al., 2008; Whittington et al., 2009).

4.4. Variation in magnetization

The composition of magnetite defines important ferromagnetic components in pyroclastic grains. These fragments are an intermediate member of the magnetite-ulvöspinel solid solution series, characterized by a significantly lower Curie point (Piper et al., 2002). Ilmenite and Ti-poor magnetite are primarily produced through oxidation caused by posteruptive processes

and/or hydrothermal fluids with a high oxygen fugacity during the cooling stage of pyroclastic products (Butler, 1998; Piper et al., 2002; Çubukçu, 2015). Furthermore, the elemental abundance of Ti in Fe-Ti oxides can alter dramatically to accommodate changes in the ambient temperature and fugacity (Devine et al., 2003; Çubukçu, 2015). Oxidation mainly originates from the initial cooling stage of magmatic products, and the crystallization of mineral phases and vapor phase diffusion occur during this process. This oxidation primarily affects the magnetic properties of minerals through textural variations in grains, characterized by Ti-rich and Ti-poor zones, leading to changes in saturation magnetization and Curie temperature depending on the chemical composition (Butler, 1998; Çubukçu, 2015). The oxidation of ferromagnetic species mainly results in the rearrangement of magnetic grain sizes. Consequently, paramagnetic zones often surround magnetic grains, causing a decrease in saturation magnetization (Piper et al., 2002; Çubukçu, 2015).

The thermomagnetic behavior of pumice samples is dominantly influenced by the composition of oxides (Le Pennec et al., 1998; Piper et al., 2002; Ghiorso and Evans, 2008). The cooling process can rapidly oxidize pumice, thereby easily affecting the magnetic behavior of the pumice sample. Oxidation leads to the generation of different bands, characterized by dark and light parts within the same pumice body (Ozima et al., 2003). The occurrence of bands in this study serves as a clear example of oxidation. Additionally, the saturation magnetization behavior observed between the dark and light bands of the pumice fall deposits explains the distribution of Fe-Ti oxides (Lawson et al., 1987; Hoffmann and Fehr, 1996). Thermomagnetic magnetization with a composition close to pure magnetite mostly displays a curve with a tail that indicates the amount of the residual paramagnetic phase (Piper et al., 2002; Ozima et al., 2003). Most of the time, the curve continues from 550 °C, resulting in a distinct Curie point of the Fe-oxide phase, as evidenced by this short linear segment at around 300 °C, with the following cusp implying oxidation shortly after cooling (Piper et al., 2002). The thermomagnetic curves of dark and light pumice bands display slightly different patterns. The light band is characterized by low-Ti titanomagnetite, while the dark bands contain nearly pure magnetite with a distinct tail of oxidation. The increase in oxidation is represented by exsolved Fe-Ti oxides with paramagnetic Ti-rich exsolutions within the dark bands, while low oxidation shows the highest level of magnetization saturation.

4.5. A general model for magma vesiculation and crystallization of banded pumice

It is possible to interpret the similarities and variations in their degassing behavior by comparing the vesicle

texture within the different pumice clasts. Additionally, the fragmentation behavior of erupted clast can indicate variations in density distribution and the amount of degassing. Variations in bulk H₂O content may also reflect different fragmentation histories and overall decompression times. Furthermore, erupted clasts containing oxide microlites can contribute to continuous nucleation. These crystals, especially magnetite, play a significant role in reducing the level of supersaturation required to initiate nucleation (Gualda and Ghiorso, 2007). The predomination of magnetite microlites in a pumice clast can particularly point to heterogeneous crystallization during magma degassing (Shea et al., 2010; 2012; Shea, 2017). However, differences within the erupted material may also emphasize the lateral and/or vertical gradients in vesicle size and crystal concentration (D’Orlando et al., 2011; Shea, 2017; Mitchell et al., 2019). Accordingly, Mitchell et al. (2019) studied the giant pumices formed in the Le Havre eruption and suggested that the microlites were formed due to the sudden cooling at the conduit walls of the ascending magma, whereby this crystal-rich part was engulfed by the lower viscosity, crystal-poor magma, and chemically homogeneous pumice bands were formed by the mingling of microlite-poor and microlite-rich parts.

Di Genova et al. (2020) stated that the presence of magnetite within an ascending magma mass might suddenly and significantly increase the viscosity of the magma. This increase may even drive an explosive eruption of low-viscosity basaltic magma. Our study reveals that the dark bands have magnetite, while the light bands have no magnetic anomalies attributed to the magnetite particles, and this heterogeneity is consistent even within the same pumice clast. Similar observations were made by Yoshida et al. (2022) in their study on pumice clasts from the 2021 Fukutoku-Oka-no-Ba eruption (Japan). They described gray and black pumices as being present evenly within the same clast. They also noted that the vesicles of gray pumice are longer, whereas the those of black pumice are more rounded. Furthermore, they found that black pumice exhibited magnetite peaks in Raman spectroscopy, corresponding to the magnetite nanolites. In our study, we demonstrated that magnetite was abundant in the groundmass of dark bands, along with crystal enrichment, compared to light bands (Figure 12).

The interesting point is that our dark and light bands exhibit no bulk chemical differences. Theoretical viscosity values, calculated from the lighter-colored band with a lower mineral content, are relatively higher. Conversely, the theoretical viscosity values of dark bands are lower. However, we cannot constrain the diversity of viscosity across the pumice bands, which could be attributed to the crystal cargo and excess Fe-oxides. The combination of millimeter- to centimeter-sized bands in pumice,

displaying noticeably diverse cooling and crystallization histories, points to the mingling of various magma regions in the conduit with variable cooling rates (Shea et al., 2012; Mitchell et al., 2019). While the VSD and chemical composition values are very similar, banding suggests the concepts of mineral segregation and melt immiscibility at this point. Considering that the crystal cargo content is the only difference, we think such a differentiation exists, particularly within the conduit under melt flow dynamics. Due to the near-surface oxidation of magnetic particles during cooling, distinct magnetic behaviors are observed in both pumice bands. As oxidation produces a distinct thermomagnetic signature for each pumice band, we subsequently consider it a potential banding mechanism.

5. Conclusion

X-ray computed tomography was carried out on six banded pumice cuts from the original pumice sample. The 3D data obtained from high-resolution image stacks were compiled to analyze vesicle and crystal characteristics. Vesicles have heterogeneous distributions with different morphologies ranging from 10 μm to 1.5 mm (with a bulk range up to 3 mm). The results of the computed tomography study further reveal that the vesicle sizes in both bands display the same distribution pattern with a mode at 150 μm . The differences in vesicle sizes are mainly attributed to several degassing pulses, rather than a single vesiculation event. Coalescence could be the primary process occurring between juxtaposed vesicles of any size to generate larger ones during the eruption decompression. This process also results in greater interconnectivity compared to the small vesicles (Whitham and Sparks, 1986; Klug and Cashman, 1994). Analysis via X-ray tomography of banded pumice

clasts reveals a accumulation of crystals, particularly oxides, within the dark band. Additionally, the light and dark pumice bands are characterized by nearly identical compositions. All examined bands display rhyolitic glass compositions accompanied by assemblages of minerals. The petrographic observations from scanning electron microscopy also reveal that dark pumice bands contain plagioclase, quartz, orthopyroxene, and magnetite (+/- pyrite), while light pumice bands consist only of plagioclase and quartz. Most of the phenocrysts (>400 μm) are fragmented due to the rapid degassing of magma through the conduit. Oxides primarily form as embedded crystals within the glassy matrix. The formation of these crystals is attributed to their wet surface attachment under magmatic conditions (Gualda and Anderson, 2007). Crystal-vesicle surface interactions dominantly favor this attachment. Crystal aggregation, preferentially of oxides, occurs as vesicles become neutrally buoyant (Gualda and Anderson, 2007). We suggest that the response of the crystals to the buoyancy forces of ascending magma may involve separation and enrichment in their flow patterns, thereby preventing homogenization and creating a degree of a mechanical immiscibility of the layers.

Acknowledgment

This study has benefited from TÜBİTAK (The Scientific and Technological Research Council of Türkiye) YDABÇAG-108Y063 and 107Y333 research projects. Additionally, it has received support from the Hacettepe University Scientific Research Projects (BAP) Coordination Unit under project no: 0701602009.2011. The authors would like to thank the anonymous reviewers for their constructive comments which enhanced the quality of the manuscript.

References

- Andrews BJ, Manga M (2014). Thermal and rheological controls on the formation of mafic enclaves or banded pumice. *Contributions to Mineralogy and Petrology* 167: 961. <https://doi.org/10.1007/s00410-013-0961-7>
- Bacon C (1986). Magmatic inclusions in silicic and intermediate volcanic rocks. *Journal of Geophysical Research* 91: 6091–6112. <https://doi.org/10.1029/JB091iB06p06091>
- Bardelli L, Arnosio M, Báez W, Suzaño N, Becchio R et al. (2020). Multi-banded pumice in the Campo de la Piedra Pómez rhyolitic ignimbrite (Southern Puna plateau): Pre-eruptive physical and chemical interactions between mafic and rhyolitic melts. *Journal of South American Earth Science* 101: 102616. <https://doi.org/10.1016/j.jsames.2020.102616>
- Baker DR, Brun F, O'Shaughnessy C, Mancini L, Fife JL et al. (2012a). A four-dimensional X-ray tomographic microscopy study of bubble growth in basaltic foam. *Nature Communications* 3: 1135. <https://doi.org/10.1038/ncomms2134>
- Baker D, Mancini L, Polacci M, Higgins M, Gualda G et al. (2012b). An introduction to the application of X-ray microtomography to the three-dimensional study of igneous rocks. *Lithos* 148: 262–276. <https://doi.org/10.1016/j.lithos.2012.06.008>
- Berg S, Troll V, Deegan F, Burchardt S, Krumbholz M et al. (2016). Heterogeneous vesiculation of 2011 El Hierro xeno-pumice revealed by X-ray computed microtomography. *Bulletin of Volcanology* 78: 85. <https://doi.org/10.1007/s00445-016-1080-x>
- Bernard O, Bouvet de Maisonneuve C, Arbaret L, Nagashima K, Oalman J et al. (2022). Varying processes, similar results: How composition influences fragmentation and subsequent feeding of large pyroclastic density currents. *Frontiers in Earth Science* 10: 979210. <https://doi.org/10.3389/feart.2022.979210>
- Bigazzi G, Yeğingil Z, Ercan T, Oddone M, Özdoğan M (1997). Age determination of obsidian bearing volcanics in Eastern Anatolia using the fission track dating method. *Geological Bulletin of Turkey* 40(2): 57–73.

- Blundy, J., Cashman, K., 2008. Petrologic reconstruction of magmatic system variables and processes. *Reviews in Mineralogy and Geochemistry* 69: 179–239. <http://doi.org/10.2138/rmg.2008.69.6>
- Butler R, Banerjee SK (1975). Theoretical single-domain grain size range in magnetite and titanomagnetite. *Journal of Geophysical Research* 80: 4049–4058. <https://doi.org/10.1029/JB080i029p04049>
- Butler RF (1998). *Paleomagnetism: Magnetic Domains to Geologic Terranes*. Blackwell Scientific Publications, Oxford, pp. 319.
- Candela PA (1986). The Evolution of Aqueous Vapor from Silicate Melts—Effect on Oxygen Fugacity. *Geochimica et Cosmochimica Acta* 50(6): 1205–1211. [https://doi.org/10.1016/0016-7037\(86\)90403-5](https://doi.org/10.1016/0016-7037(86)90403-5)
- Cashman KV (2020). Crystal Size Distribution (CSD) Analysis of Volcanic Samples: Advances and Challenges. *Frontiers in Earth Science* 8: 291. <https://doi.org/10.3389/feart.2020.00291>
- Cashman KV, Mangan MT (1994). Physical aspects of magmatic degassing II. Constraints on vesiculation processes from textural studies of eruptive products. In: Carroll, M.R., Holloway, J.R. (Eds.), *Volatiles in Magmas*. American Mineralogist, Chantilly, pp. 447–478.
- Clynne MA (1999). A complex magma mixing origin for rocks erupted in 1915, Lassen Peak, California. *Journal of Petrology* 40(1): 105–132. <https://doi.org/10.1093/ptro/40.1.105>
- Coombs ML, Eichelberger JC, Rutherford MJ (2000). Magma storage and mixing conditions for the 1953–1974 eruptions of Southwest Trident Volcano, Katmai National Park, Alaska. *Contributions to Mineralogy and Petrology* 140: 99–118. <https://doi.org/10.1007/s004100000166>
- Couch S, Sparks RSJ, Carroll MR (2003). The Kinetics of Degassing-Induced Crystallization at Soufrière Hills Volcano, Montserrat. *Journal of Petrology* 44(8): 1477–1502. <https://doi.org/10.1093/ptro/44.8.1477>
- Çubukçu HE (2015). Vertical variation in the deuteric oxidation of titanomagnetites in an ignimbrite deposit: Kizilkaya Ignimbrite (Cappadocia, Turkey). *Journal of Volcanology and Geothermal Research* 308: 10–15. <https://doi.org/10.1016/j.jvolgeores.2015.10.006>
- Deniel C, Aydar E, Gourgaud A (1998). The Hasan Dagi stratovolcano (Central Anatolia, Turkey): Evolution from calc-alkaline to alkaline magmatism in a collision zone. *Journal of Volcanology and Geothermal Research* 87(1-4): 275–302. [https://doi.org/10.1016/S0377-0273\(98\)00097-3](https://doi.org/10.1016/S0377-0273(98)00097-3)
- Devine JD, Rutherford MJ, Norton GE, Young SR (2003). Magma storage region processes inferred from geochemistry of Fe–Ti oxides in andesitic magma, Soufriere Hills Volcano, Montserrat, WI. *Journal of Petrology* 44(8): 1375–1400. <https://doi.org/10.1093/ptro/44.8.1375>
- Dhont D, Chorowicz J, Yürür T, Froger JL, Köse, O et al. (1998). Emplacement of volcanic vents and geodynamics of Central Anatolia, Turkey. *Journal of Volcanology and Geothermal Research* 85: 33–54. [https://doi.org/10.1016/S0377-0273\(98\)00048-1](https://doi.org/10.1016/S0377-0273(98)00048-1)
- Di Genova D, Brooker RA, Mader HM, Drewitt JW, Longo A et al. (2020) In situ observation of nanolite growth in volcanic melt: A driving force for explosive eruptions. *Science Advances* 6(39): eabb0413. <https://doi.org/10.1126/sciadv.abb0413>
- Dirik K, Göncüoğlu MC (1996). Neotectonic characteristics of Central Anatolia. *International Geology Review* 38: 807–817. <https://doi.org/10.1080/00206819709465363>
- Dogan-Kulahci GD, Temel A, Gourgaud A, Varol E, Guillou H et al. (2018). Contemporaneous alkaline and calc-alkaline series in Central Anatolia (Turkey): Spatio-temporal evolution of a post-collisional Quaternary basaltic volcanism. *Journal of Volcanology and Geothermal Research* 356: 56–74. <https://doi.org/10.1016/j.jvolgeores.2018.02.012>
- D’Orlando C, Cioni R, Bertagnini A, Andronico D, Cole PD (2011). Dynamics of ash-dominated eruptions at Vesuvius: the post-512 AD AS1a event. *Bulletin of Volcanology* 73: 699–715. <https://doi.org/10.1007/s00445-010-0432-1>
- Druitt TH, Brechley PJ, Gökteni YE, Francaviglia V (1995). Late Quaternary rhyolitic eruptions from the Acigöl Complex, central Turkey. *Journal of Geological Society (London)* 152: 655–667. <https://doi.org/10.1144/gsjgs.152.4.0655>
- Eichelberger JC (1980). Vesiculation of mafic magma during replenishment of silicic reservoirs. *Nature* 288: 446–450. <https://doi.org/10.1038/288446a0>
- Eichelberger JC, Chertkoff DC, Dreher ST, Nye CJ (2000). Magmas in collision: rethinking chemical zonation in silicic magmas. *Geology* 28: 603–606. [https://doi.org/10.1130/0091-7613\(2000\)28<603:MICRCZ>2.0.CO;2](https://doi.org/10.1130/0091-7613(2000)28<603:MICRCZ>2.0.CO;2)
- Giachetti T, Burgisser A, Arbaret L, Druitt TH, Kelfoun K (2011). Quantitative textural analysis of Vulcanian pyroclasts (Montserrat) using multi-scale X-ray computed microtomography: comparison with results from 2D image analysis. *Bulletin of Volcanology* 73: 1295–1309. <http://doi.org/10.1007/s00445-011-0472-1>
- Giordano D, Russell JK, Dingwell DB (2008). Viscosity of magmatic liquids: a model. *Earth and Planetary Science Letters* 271: 123–134. <https://doi.org/10.1016/j.epsl.2008.03.038>
- Ghiorso MS, Evans BW (2008). Thermodynamics of rhombohedral oxide solid solutions and a revision of the Fe–Ti two-oxide geothermometer and oxygen-barometer. *American Journal of Science* 30 (9): 957–1039. <https://doi.org/10.2475/09.2008.01>
- Gonnermann HM, Manga M (2005). Flow banding in obsidian: A record of evolving textural heterogeneity during magma deformation. *Earth and Planetary Science Letters* 236: 135–147. <https://doi.org/10.1016/j.epsl.2005.04.031>
- González-García D, Petrelli M, Perugini D, Giordano D, Vasseur J et al. (2022). Pre-Eruptive Conditions and Dynamics Recorded in Banded Pumices from the El Abrigo Caldera-Forming Eruption (Tenerife, Canary Islands). *Journal of Petrology* 63(3): egac009. <https://doi.org/10.1093/ptro/egac009>
- Gualda GAR, Cook DL, Chopra R, Qin LP, Anderson AT et al. (2004). Fragmentation, nucleation and migration of crystals and bubbles in the Bishop Tuff rhyolitic magma. *Earth and Environmental Transactions of the Royal Society of Edinburgh* 95: 375–390. <https://doi.org/10.1017/S0263593300001139>

- Gualda GAR (2006). Crystal size distributions derived from 3D datasets: Sample size versus uncertainties. *Journal of Petrology* 47(6): 1245–1254. <https://doi.org/10.1093/petrology/egl010>
- Gualda GAR, Anderson AT (2007). Magnetite scavenging and the buoyancy of bubbles in magmas. Part 1: Discovery of a pre-eruptive bubble in Bishop rhyolite. *Contributions to Mineralogy and Petrology* 153(6), 733–742. <https://doi.org/10.1007/s00410-006-0173-5>
- Gualda GAR, Ghiorso MS (2007). Magnetite scavenging and the buoyancy of bubbles in magmas. Part 2: Energetics of crystal-bubble attachment in magmas. *Contributions to Mineralogy and Petrology* 154: 479–490. <https://doi.org/10.1007/s00410-007-0206-8>
- Gualda GAR, Rivers M (2006). Quantitative 3D petrography using X-ray tomography: Application to Bishop Tuff pumice clasts. *Journal of Volcanology and Geothermal Research* 154(1–2): 48–62. <https://doi.org/10.1016/j.jvolgeores.2005.09.019>
- Guntoro PI, Ghorbani Y, Koch P-H, Rosenkranz J (2019). X-ray Microcomputed Tomography (μ CT) for Mineral Characterization: A Review of Data Analysis Methods. *Minerals* 9(3): 183. <https://doi.org/10.3390/min9030183>
- Gurioli L, Harris AJL, Houghton BF, Polacci M, Ripepe M (2008). Textural and geophysical characterization of explosive basaltic activity at Villarrica volcano. *Journal of Geophysical Research* 113. <https://doi.org/10.1029/2007JB005328>
- Hersum TG, Marsh BD (2007). Igneous textures: on the kinetics behind the words. *Elements* 3: 247–252
- Hoffmann V, Fehr KTH (1996). Micromagnetic, rockmagnetic and mineralogical studies on dacitic pumice from the Pinatubo eruption (1991, Philippines) showing self-reversed TRM. *Geophysical Research Letters* 23: 2835–2838. <https://doi.org/10.1029/96GL01317>
- Iacovino K, Till CB (2019). DensityX: A program for calculating the densities of magmatic liquids up to 1,627 °C and 30 kbar. *Volcanica* 2(1): 1–10. <https://doi.org/10.30909/vol.02.01.0110>
- Innocenti F, Mazzuoli R, Pasquarè G, Radicati Di Brozolo F, Villari L (1975). The Neogene calcalkaline volcanism of Central Anatolia: geochronological data on Kayseri–Nigde area. *Geological Magazine* 112: 349–360. <https://doi.org/10.1017/S0016756800046744>
- Klug C, Cashman KV (1994). Vesiculation of May 18, 1980, Mount St. Helens magma. *Geology* 22(5): 468–472. [https://doi.org/10.1130/0091-7613\(1994\)022<0468:VOMMSH>2.3.CO;2](https://doi.org/10.1130/0091-7613(1994)022<0468:VOMMSH>2.3.CO;2)
- Klug C, Cashman K, Bacon C (2002). Structure and physical characteristics of pumice from the climactic eruption of Mount Mazama (Crater Lake), Oregon. *Bulletin of Volcanology* 64: 486–501. <https://doi.org/10.1007/s00445-002-0230-5>
- Koyaguchi T (1985). Magma mixing in a volcanic conduit. *Journal of Volcanology and Geothermal Research* 25: 365–369.
- Koyaguchi T (1986). Evidence for two-stage mixing in magmatic inclusions and rhyolitic lava domes on Niiijima Island, Japan. *Journal of Volcanology and Geothermal Research* 29: 71–98.
- Lawson CA, Nord Jr. GL, Champion DE (1987). Fe-Ti oxide mineralogy and the origin of normal and reverse remanent magnetization in dacitic pumice blocks from Mt. Shasta, California. *Physics of the Earth and Planetary Interiors* 46: 270–288. [https://doi.org/10.1016/0031-9201\(87\)90190-7](https://doi.org/10.1016/0031-9201(87)90190-7)
- Le Bas MJ, Lemaitre RW, Streckeisen A, Zanettin B (1986). A Chemical Classification of Volcanic-Rocks Based on the Total Alkali Silica Diagram. *Journal of Petrology* 27(3): 745–750.
- Le Pennec JL, Bourdier JL, Forger JL, Temel A, Camus G et al. (1994). Neogene ignimbrites of the Nevşehir plateau (Central Turkey): stratigraphy, distribution, and source constraints. *Journal of Volcanology and Geothermal Research* 63: 59–87. [https://doi.org/10.1016/0377-0273\(94\)90018-3](https://doi.org/10.1016/0377-0273(94)90018-3)
- Le Pennec JL, Chen Y, Diot H, Froger JL, Gourgaud A (1998). Interpretation of anisotropy of magnetic susceptibility fabric of ignimbrites in terms of kinematic and sedimentological mechanisms: An Anatolian case-study. *Earth and Planetary Science Letters* 157(1–2): 105–127. [https://doi.org/10.1016/S0012-821X\(97\)00215-X](https://doi.org/10.1016/S0012-821X(97)00215-X)
- Leslie-Pelecky D, Rieke R (1996). Magnetic Properties of Nanostructured Materials. *Chemistry of Materials* 8: 1770–1783. <https://doi.org/10.1021/cm960077f>
- Li Q, Kartikowati CW, Horie S, Ogi T, Iwaki T et al. (2017). Correlation between particle size/domain structure and magnetic properties of highly crystalline Fe₃O₄ nanoparticles. *Scientific Reports* 7: 9894. <https://doi.org/10.1038/s41598-017-09897-5>
- Ling-fei CAO, Dan XIE, Ming-xing GUO, Park HS, Fujita T (2007). Size and shape effects on Curie temperature of ferromagnetic nanoparticles. *Transactions of Nonferrous Metal Society of China* 17(6): 1451–1455. [https://doi.org/10.1016/S1003-6326\(07\)60293-3](https://doi.org/10.1016/S1003-6326(07)60293-3)
- Liedl A, Buono G, Lanzafame G, Dabagov S, Hampai D et al. (2019). A 3D imaging textural characterization of pyroclastic products from the 1538 CE Monte Nuovo eruption (Campi Flegrei, Italy). *Lithos* 340: 316–331. <https://doi.org/10.1016/j.lithos.2019.05.010>
- Marsh BD (2007). Crystallization of silicate magmas deciphered using crystal size distributions. *Journal of American Ceramic Society* 90: 746–757. <https://doi.org/10.1111/j.1551-2916.2006.01473.x>
- Miller JD, Lin CL, Cortes AB (1990). A review of X-ray computed tomography and its applications in mineral processing. *Mineral Processing and Extractive Metallurgy Review* 7(1): 1–18. <https://doi.org/10.1080/08827509008952663>
- Mitchell SJ, Houghton BF, Carey RJ, Manga M, Fauria KE et al. (2019). Submarine giant pumice: a window into the shallow conduit dynamics of a recent silicic eruption. *Bulletin of Volcanology* 81: 42. <https://doi.org/10.1007/s00445-019-1298-5>
- Moitra P, Gonnermann HM, Houghton BF, Giachetti T (2013). Relating vesicle shapes in pyroclasts to eruption styles. *Bulletin of Volcanology* 75: 691. <https://doi.org/10.1007/s00445-013-0691-8>

- Mouralis D, Pastre JF, Kuzucuoglu C, Türkecan A, Guilloue H (2019). Tephrostratigraphy and chronology of the Quaternary Göllüdağ and Acıgöl volcanic complexes (Central Anatolia, Turkey). *Mediterranean Geoscience Reviews* 1: 179–202. <https://doi.org/10.1007/s42990-019-00010-8>
- Noguchi S, Toramaru A, Nakada S (2008). Relation between microlite textures and discharge rate during the 1991–1995 eruptions at Unzen, Japan. *Journal of Volcanology and Geothermal Research* 175(1–2): 141–155. <https://doi.org/10.1016/j.jvolgeores.2008.03.025>
- Ozima M, Oshima O, Funaki M (2003). Magnetic properties of pyroclastic rocks from the later stage of the eruptive activity of Haruna Volcano in relation to the self-reversal of thermoremanent magnetization. *Earth, Planets and Space* 55: 183–188. <https://doi.org/10.1186/BF03351747>
- Özsayın E, Çiner A, Rojay B, Dirik K, Melnick D (2013). Plio-Quaternary extensional tectonics of the Central Anatolian Plateau: a case study from the Tuz Gölü Basin, Turkey. *Turkish Journal of Earth Science* 22: 691–714. <http://doi.org/10.3906/yer-1210-5>
- Piochi M, Polacci M, De Astis G, Zanetti A, Mangiacapra A et al. (2008). Texture and composition of pumices and scoriae from the Campi Flegrei caldera (Italy): Implications on the dynamics of explosive eruptions. *Geochemistry, Geophysics, Geosystems* 9: Q03013. <https://doi.org/10.1029/2007GC001746>
- Piper JDA, Gürsoy H, Tatar O (2002). Palaeomagnetism and magnetic properties of the Cappadocian ignimbrite succession, central Turkey and Neogene tectonics of the Anatolian collage. *Journal of Volcanology and Geothermal Research* 117(3–4): 237–262. [https://doi.org/10.1016/S0377-0273\(02\)00221-4](https://doi.org/10.1016/S0377-0273(02)00221-4)
- Polacci M, Papale P, Rosi M (2001). Textural heterogeneities in pumices from the climactic eruption of Mount Pinatubo, 15 June 1991, and implications for magma ascent dynamics. *Bulletin of Volcanology* 63(2–3): 83–97. <https://doi.org/10.1007/s004450000123>
- Polacci M, Papale P, Del Seppia D, Giordano D, Romano C (2004). Dynamics of magma ascent and fragmentation in trachytic versus rhyolitic eruptions. *Journal of Volcanology and Geothermal Research* 131(1–2): 93–108. [https://doi.org/10.1016/S0377-0273\(03\)00319-6](https://doi.org/10.1016/S0377-0273(03)00319-6)
- Polacci M, Arzilli F, La Spina G, Le Gall N, Cai B et al. (2018). Crystallisation in basaltic magmas revealed via in situ 4D synchrotron X-ray microtomography. *Scientific Reports* 8: 8377. <https://www.nature.com/articles/s41598-018-26644-6>
- Polacci M, Mancini L, Baker DR (2010). The contribution of synchrotron X-ray computed microtomography to understanding volcanic processes soil and geosciences. *Journal of Synchrotron Radiation* 17: 215–221. <https://doi.org/10.1107/S0909049509048225>
- Reid MR, Schleiffarth WK, Cosca MA, Delph JR, Blichert-Toft J et al. (2017). Shallow melting of MORB-like mantle under hot continental lithosphere, Central Anatolia. *Geochemistry, Geophysics, Geosystems* 18(5): 1866–1888. <https://doi.org/10.1002/2016GC006772>
- Rosi M, Landi P, Polacci M, Di Muro A, Zandomenighi D (2004). Role of conduit shear on ascent of the crystal-rich magma feeding the 800-year-BP Plinian eruption of Quilotoa Volcano (Ecuador). *Bulletin of Volcanology* 66(4): 307–321. <https://doi.org/10.1007/s00445-003-0312-z>
- Schmitt AK, Danišik M, Evans NJ, Siebel W, Kiemle E (2011). Acıgöl rhyolite field, Central Anatolia (part 1): high-resolution dating of eruption episodes and zircon growth rates. *Contributions to Mineralogy and Petrology* 162: 1215–1231. <https://doi.org/10.1007/s00410-011-0648-x>
- Shea T, Houghton BF, Gurioli L, Cashman KV, Hammer JE et al. (2010). Textural studies of vesicles in volcanic rocks: An integrated methodology. *Journal of Volcanology and Geothermal Research* 190: 271–289. <https://doi.org/10.1016/j.jvolgeores.2009.12.003>
- Shea T, Gurioli L, Houghton BF (2012). Transitions between fall phases and pyroclastic density currents during the AD 79 eruption at Vesuvius: building a transient conduit model from the textural and volatile record. *Bulletin of Volcanology* 74: 2363–2381. <https://doi.org/10.1007/s00445-012-0668-z>
- Shea T (2017). Bubble nucleation in magmas: A dominantly heterogeneous process? *Journal of Volcanology and Geothermal Research* 343 (1): 155–170. <https://doi.org/10.1016/j.jvolgeores.2017.06.025>
- Smith JV (2000). Textural evidence for dilatant (shear thickening) rheology of magma at high crystal concentrations. *Journal of Volcanology and Geothermal Research* 99(1–4): 1–7. [https://doi.org/10.1016/S0377-0273\(99\)00191-2](https://doi.org/10.1016/S0377-0273(99)00191-2)
- Spera FJ (2000). Physical properties of magma. In: Sigurdsson H (ed) *Encyclopedia of volcanoes*. Academic Press, New York, pp. 171–190.
- Suhendro I, Toramaru A, Harijoko A, Wibowo HE (2022). The origins of transparent and non-transparent white pumice: A case study of the 52 ka Maninjau caldera-forming eruption, Indonesia. *Journal of Volcanology and Geothermal Research* 431: 107643. <https://doi.org/10.1016/j.jvolgeores.2022.107643>
- Şengör AMC, Yılmaz Y (1981). Tethyan evolution of Turkey: A plate tectonic approach. *Tectonophysics* 75(3–4): 181–241. [https://doi.org/10.1016/0040-1951\(81\)90275-4](https://doi.org/10.1016/0040-1951(81)90275-4)
- Toprak V, Göncüoğlu MC (1993). Tectonic control on the development of the Neogene-Quaternary Central Anatolian Volcanic Province, Turkey. *Geological Journal* 28: 357–369. <https://doi.org/10.1002/gj.3350280314>
- Toprak V (1998). Vent distribution and its relation to regional tectonics, Cappadocian Volcanics, Turkey. *Journal of Volcanology and Geothermal Research* 85(1–4): 55–67. [https://doi.org/10.1016/S0377-0273\(98\)00049-3](https://doi.org/10.1016/S0377-0273(98)00049-3)
- Toramaru A (2014). On the second nucleation of bubbles in magmas under sudden decompression. *Earth and Planetary Science Letters* 404: 190–199. <https://doi.org/10.1016/j.epsl.2014.07.035>

- Voltolini M, Zandomenighi D, Mancini L, Polacci M (2011). Texture analysis of volcanic rock samples: Quantitative study of crystals and vesicles shape preferred orientation from X-ray microtomography data. *Journal of Volcanology and Geothermal Research* 202: 83–95. <https://doi.org/10.1016/j.jvolgeores.2011.02.003>
- Waythomas CF, Scott WE, Prejean SG, Schneider DJ, Izbekov PE et al. (2010). The 7–8 August 2008 eruption of Kasatochi Volcano, central Aleutian Islands, Alaska. *Journal of Geophysical Research* 115: B00B06. <http://doi.org/10.1029/2010JB007437>
- Whitham AG, Sparks RSJ, (1986). Pumice. *Bulletin of Volcanology* 48(4): 209–223. <https://doi.org/10.1007/BF01087675>
- Whittington AG, Hellwig BM, Behrens H, Joachim B, Stechern A et al. (2009). The viscosity of hydrous dacitic liquids: implications for the rheology of evolving silicic magmas. *Bulletin of Volcanology* 71: 185–199. <https://doi.org/10.1007/s00445-008-0217-y>
- Wright HMN, Cashman KV, Gottesfeld EH, Roberts JJ (2009). Pore structure of volcanic clasts: measurements of permeability and electrical conductivity. *Earth and Planetary Science Letters* 280: 93–104. <https://doi.org/10.1016/j.epsl.2009.01.023>
- Yoshida K, Tamura Y, Sato T, Hanyu T, Usui Y et al. (2022). Variety of the drift pumice clasts from the 2021 Fukutoku-Oka-no-Ba eruption, Japan. *Island Arc* 31(1): e12441. <https://doi.org/10.1111/iar.12441>
- Zandomenighi D, Voltolini M, Mancini L, Brun F, Dreossi D et al. (2010). Quantitative analysis of X-ray microtomography images of geomaterials: Application to volcanic rocks. *Geosphere* 6(6): 793–804. <https://doi.org/10.1130/GES00561.1>

Supplementary Table 1A. Whole-rock major element of dark and light bands.

Definition	Sample no.	x_koor	y_koor	SiO ₂	Al ₂ O ₃	Fe ₂ O ₃	MgO	CaO	Na ₂ O	K ₂ O	TiO ₂	P ₂ O ₅	MnO	Cr ₂ O ₃	LOI	Total
Light band	K-056-A	632877	4245796	71.35	13.53	1.64	0.56	1.33	3.30	4.37	0.17	0.05	0.07	0.002	3.4	99.81
Dark band	K-056-B	632877	4245796	71.66	13.42	1.51	0.53	1.34	3.31	4.36	0.16	0.02	0.07	0.002	3.5	99.85

Supplementary Table 1B. Major element analysis of groundmass glass for dark and light bands.

Def.	Analysis id	Na ₂ O	MgO	Al ₂ O ₃	SiO ₂	K ₂ O	CaO	TiO ₂	MnO	FeO	Total
Dark	1	0.82	0.13	11.63	73.31	3.95	0.29	0.001	0.011	1.23	91.37
Dark	2	1.10	0.04	12.56	71.94	4.48	0.75	0.163	0.001	1.26	92.28
Dark	3	1.24	0.00	11.14	68.76	5.03	0.61	0.114	0.001	1.36	88.25
Dark	4	0.93	0.05	11.17	72.77	4.59	0.00	0.001	0.001	1.36	90.87
Dark	5	1.12	0.04	11.47	72.73	4.73	0.51	0.001	0.016	1.21	91.84
Dark	6	1.41	0.05	11.73	75.17	4.43	0.24	0.001	0.001	1.12	94.16
Dark	7	1.41	0.13	11.75	72.58	4.59	0.27	0.001	0.001	1.09	91.82
Dark	8	1.28	0.08	11.98	72.91	4.59	0.47	0.001	0.001	1.10	92.42
Dark	9	1.49	0.12	11.98	71.37	4.69	0.00	0.001	0.051	1.69	91.39
Dark	10	1.33	0.13	12.19	69.25	4.56	0.22	0.001	0.001	1.22	88.89
Dark	11	1.29	0.26	12.33	69.70	4.35	0.59	0.007	0.001	1.85	90.37
Dark	12	0.97	0.13	11.38	70.10	4.41	0.36	0.001	0.047	1.61	89.00
Dark	13	0.93	0.15	11.98	74.50	4.63	0.36	0.001	0.001	1.36	93.91
Dark	14	1.16	0.09	10.98	69.82	4.37	0.35	0.026	0.129	2.16	89.09
Dark	15	1.44	0.16	12.02	74.02	4.50	0.34	0.001	0.001	1.73	94.22
Dark	16	1.38	0.22	11.99	73.68	4.50	0.34	0.001	0.001	1.81	93.92
Dark	17	1.34	0.16	12.77	72.80	4.18	0.58	0.001	0.001	1.75	93.58
Dark	18	1.64	0.23	13.39	69.44	4.11	1.12	0.001	0.001	1.74	91.66
Dark	19	1.12	2.33	15.64	68.01	3.76	0.43	0.001	0.047	2.75	94.09
Dark	20	1.26	0.18	12.21	70.85	4.47	0.49	0.001	0.001	1.95	91.43
Dark	21	0.70	0.05	11.61	70.25	4.19	0.34	0.001	0.001	1.59	88.74
Dark	22	1.17	0.07	12.16	74.51	4.32	0.47	0.001	0.063	1.78	94.55
Dark	23	0.75	0.22	12.30	70.23	4.10	0.47	0.001	0.052	2.31	90.43
Dark	24	1.35	0.20	12.94	70.79	4.50	0.91	0.196	0.001	1.81	92.69
Dark	25	1.20	0.08	11.66	70.08	4.16	0.21	0.001	0.001	1.38	88.78
Dark	26	1.15	0.18	12.90	70.40	4.01	0.68	0.001	0.001	1.84	91.17
Dark	27	0.99	0.16	11.90	71.88	4.20	0.29	0.001	0.001	1.42	90.85
Dark	28	0.85	0.16	11.67	74.75	4.00	0.00	0.001	0.001	1.59	93.01
Dark	29	1.28	0.60	14.04	70.25	3.75	0.75	0.001	0.001	2.34	93.02
Dark	30	0.80	0.14	12.04	70.82	3.77	0.29	0.025	0.161	2.01	90.05
Light	31	0.88	0.00	11.56	73.61	3.89	0.11	0.001	0.036	1.25	91.34

Supplementary Table 1B (Continued).

Def.	Analysis id	Na ₂ O	MgO	Al ₂ O ₃	SiO ₂	K ₂ O	CaO	TiO ₂	MnO	FeO	Total
Light	32	1.00	0.03	11.74	74.44	4.08	0.49	0.029	0.003	1.11	92.93
Light	33	1.00	0.04	12.05	72.96	3.55	0.34	0.001	0.001	1.23	91.17
Light	34	0.96	0.00	11.70	73.94	4.28	0.25	0.001	0.001	1.30	92.42
Light	35	1.07	0.04	11.98	72.96	4.18	0.00	0.001	0.001	1.10	91.32
Light	36	1.04	0.02	11.97	74.52	3.88	0.32	0.001	0.001	0.84	92.59
Light	37	1.05	0.05	12.45	75.29	3.99	0.00	0.001	0.001	1.11	93.93
Light	38	1.04	0.02	11.81	72.34	4.05	0.00	0.001	0.001	0.86	90.13
Light	39	1.32	0.06	12.94	72.16	3.89	0.67	0.001	0.001	1.09	92.12
Light	40	0.97	0.02	11.60	71.43	3.81	0.21	0.001	0.072	1.30	89.42
Light	41	1.04	0.04	11.91	75.18	4.08	0.21	0.001	0.001	1.09	93.55
Light	42	1.10	0.02	11.96	76.75	3.89	0.00	0.001	0.001	1.07	94.80
Light	43	1.08	0.04	11.57	73.80	4.11	0.47	0.001	0.001	1.38	92.46
Light	44	0.93	0.03	12.04	75.10	3.93	0.00	0.001	0.001	0.74	92.79
Light	45	0.92	0.00	12.04	75.53	4.51	0.71	0.102	0.104	1.14	95.06
Light	46	1.11	0.00	11.75	73.27	4.19	0.00	0.001	0.007	1.03	91.36
Light	47	1.15	0.07	12.43	74.83	4.59	0.64	0.467	0.072	1.18	95.42
Light	48	1.27	0.01	12.82	75.45	4.95	0.74	0.219	0.139	1.28	96.88
Light	49	0.90	0.00	12.29	72.89	4.10	0.31	0.001	0.001	1.29	91.79
Light	50	1.13	0.01	12.31	76.46	4.36	0.72	0.382	0.088	1.50	96.97
Light	51	1.18	0.06	12.76	75.61	3.64	0.00	0.001	0.001	1.17	94.42
Light	52	1.19	0.07	12.16	75.31	3.69	0.00	0.001	0.090	1.24	93.75
Light	53	1.02	0.00	11.86	73.08	4.21	0.00	0.001	0.056	0.97	91.20
Light	54	1.00	0.00	11.78	74.14	4.18	0.00	0.001	0.001	0.85	91.95
Light	55	1.06	0.00	11.85	74.87	4.00	0.20	0.001	0.001	1.65	93.63
Light	56	0.96	0.02	11.81	73.88	4.08	0.20	0.001	0.001	1.17	92.12
Light	57	1.27	0.04	12.18	74.04	4.23	0.32	0.001	0.055	1.79	93.94
Light	58	0.98	0.00	11.88	72.88	4.52	0.43	0.001	0.001	1.32	92.00
Light	59	0.87	0.00	11.65	74.00	4.18	0.00	0.001	0.001	1.08	91.78
Light	60	0.98	0.01	11.91	73.17	4.36	0.56	0.257	0.001	1.07	92.32

Supplementary Table 2A. Mineral analysis of dark and light bands (feldspar).

Def.	Mineral	Analysis loc.	Size	Analysis id	Na ₂ O	MgO	K ₂ O	CaO	TiO ₂	FeO _t	MnO	SiO ₂	Al ₂ O ₃	Total
Dark	Fld	c	130	1	6.00	0.0030	0.77	5.02	0.0037	0.005	0.004	65.43	23.65	100.89
Dark	Fld	r	130	2	5.75	0.0030	1.02	5.98	0.0110	0.012	0.005	65.60	24.56	102.94
Dark	Fld	c	156	9	4.50	0.0005	0.53	9.53	0.0640	0.318	0.001	60.61	26.84	102.40
Dark	Fld	r	156	10	3.16	0.0029	1.30	9.94	0.4131	0.005	0.004	59.44	25.28	99.54
Dark	Fld	c	172.2	11	5.11	0.0029	0.85	7.16	0.0039	0.005	0.004	60.66	23.99	97.79
Dark	Fld	r	172.2	12	4.33	0.0030	0.49	8.47	0.0039	0.005	0.005	62.68	26.25	102.23
Dark	Fld	c	58.42	13	3.23	0.0030	0.87	12.83	0.5621	0.004	0.004	57.38	27.85	102.73
Dark	Fld	r	58.42	14	2.51	0.0030	0.86	12.70	0.1083	0.005	0.004	57.32	29.11	102.61
Dark	Fld	c	93.23	15	2.46	0.0003	0.43	11.82	0.0004	0.648	0.002	54.91	28.42	98.68
Dark	Fld	r	93.23	16	3.29	0.0003	1.56	8.77	0.0005	1.052	0.023	59.35	23.98	98.03
Dark	Fld	c	280	17	5.23	0.0003	1.26	5.97	0.0004	0.484	0.070	61.29	23.08	97.39
Dark	Fld	r	280	18	4.92	0.0003	1.07	6.98	0.0242	0.461	0.001	61.36	24.06	98.89
Dark	Fld	c	99.19	19	3.48	0.0003	1.12	9.82	0.0004	0.780	0.030	58.02	26.43	99.68
Dark	Fld	r	99.19	20	3.24	0.0003	1.10	10.05	0.0005	0.818	0.001	57.90	26.59	99.71
Dark	Fld	c	159.5	21	4.13	0.0003	1.18	8.46	0.1168	0.377	0.001	60.18	25.49	99.93
Dark	Fld	r	159.5	22	4.10	0.0003	1.30	8.27	0.0226	0.523	0.001	61.34	25.23	100.78
Dark	Fld	c	169.6	25	0.77	0.0769	3.69	0.13	0.0262	1.331	0.001	61.83	33.75	101.59
Dark	Fld	r	169.6	26	2.95	0.0048	3.85	3.14	0.0530	1.186	0.225	69.16	18.08	98.65
Dark	Fld	c	332.4	27	6.78	0.0003	1.41	3.30	0.2399	0.344	0.001	65.51	20.92	98.50
Dark	Fld	r	332.4	28	6.22	0.0003	1.47	3.53	0.0005	0.144	0.001	64.84	20.82	97.03
Dark	Fld	c	381.9	29	3.61	0.0003	1.08	9.55	0.0217	0.120	0.001	59.48	27.01	100.87
Dark	Fld	r	381.9	30	3.69	0.0004	1.41	8.33	0.0665	0.562	0.001	59.63	25.38	99.06
Dark	Fld	c	385.8	31	4.26	0.0004	7.30	0.84	0.3485	0.378	0.146	68.67	18.38	100.32
Dark	Fld	r	385.8	32	3.64	0.0004	3.96	2.95	0.0005	0.856	0.101	68.31	18.21	98.03
Light	Fld	c	500	34	3.33	0.0003	0.78	10.10	0.0004	0.563	0.001	57.35	26.56	98.69
Light	Fld	r	500	35	3.54	0.0003	0.88	9.86	0.0004	0.763	0.053	57.43	26.13	98.66
Light	Fld	c	459.8	36	3.15	0.0003	0.72	11.09	0.0005	0.681	0.001	56.64	27.54	99.81
Light	Fld	r	459.8	37	3.15	0.0003	0.98	9.63	0.0004	0.797	0.001	58.51	25.91	98.98
Light	Fld	c	251.3	38	4.56	0.0003	7.57	0.62	0.2474	0.248	0.103	69.58	18.63	101.56
Light	Fld	r	251.3	40	3.29	0.0003	3.41	3.18	0.0032	0.959	0.072	68.02	18.85	97.79
Light	Fld	c	215.3	41	4.34	0.0003	5.88	1.18	0.1023	0.508	0.093	68.03	17.95	98.09
Light	Fld	r	215.3	42	4.62	0.0003	4.61	2.08	0.0151	0.333	0.000	68.70	18.16	98.52
Light	Fld	c	122.9	43	4.44	0.0003	1.33	7.73	0.0004	0.428	0.001	59.58	24.28	97.78
Light	Fld	r	122.9	44	4.48	0.0003	1.28	7.60	0.0004	0.653	0.050	59.37	24.23	97.66
Light	Fld	c	139.6	45	6.16	0.0003	0.71	4.74	0.0005	0.177	0.001	64.83	22.54	99.15
Light	Fld	r	139.6	46	5.55	0.0003	0.99	5.48	0.0005	0.172	0.001	63.68	22.21	98.09
Light	Fld	c	143.6	49	6.63	0.0004	1.32	3.07	0.0005	0.453	0.259	66.52	21.07	99.32
Light	Fld	r	143.6	50	5.44	0.0004	2.02	4.19	0.0005	0.116	0.001	66.71	21.01	99.50
Light	Fld	c	301.5	52	4.83	0.0004	6.55	1.06	0.0963	0.431	0.109	69.67	18.50	101.23
Light	Fld	r	301.5	53	3.46	0.0004	3.64	3.38	0.1630	0.997	0.001	67.95	17.96	97.54
Light	Fld	c	72.15	71	2.31	0.0005	0.45	13.34	0.0006	0.843	0.001	53.56	29.21	99.71
Light	Fld	r	72.15	72	3.04	0.0004	0.65	10.93	0.0006	0.899	0.065	56.27	27.08	98.95
Light	Fld	c	205.9	73	5.37	0.0005	0.93	7.15	0.4062	0.127	0.001	62.28	23.36	99.25
Light	Fld	r	205.9	74	4.83	0.0005	1.19	7.26	0.0918	0.253	0.001	60.27	26.22	101.07
Light	Fld	c	252.2	75	4.62	0.0005	0.63	8.76	0.0006	0.478	0.081	60.27	26.22	101.07
Light	Fld	r	252.2	76	4.38	0.0005	1.09	7.89	0.1325	0.307	0.001	61.16	24.38	99.33
Light	Fld	c	86.09	77	3.48	0.0005	1.19	10.08	0.0007	0.655	0.001	58.76	25.99	100.15
Light	Fld	r	86.09	78	3.35	0.0005	1.07	9.89	0.0007	0.627	0.001	59.00	26.39	100.33

Supplementary Table 2B. Mineral analysis of dark and light bands (pyroxene).

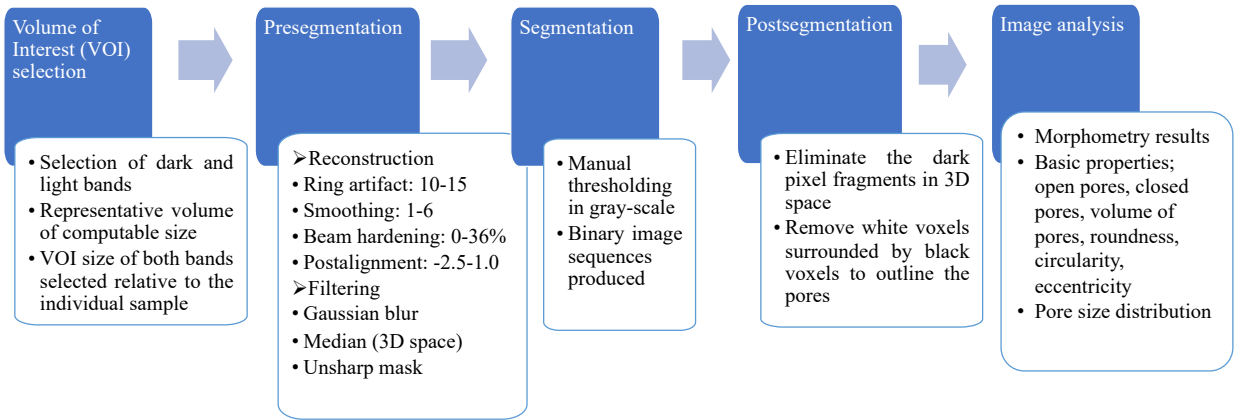
Def.	Mineral	Analysis loc.	Size	Analysis id	Na ₂ O	MgO	K ₂ O	CaO	TiO ₂	FeO _t	MnO	SiO ₂	Al ₂ O ₃	Total
Dark	Prx	c		54	0.0004	30.06	0.0002	0.0003	0.0004	10.27	0.3725	58.04	2.56	101.31
Dark	Prx	r		55	0.0004	23.31	0.7409	0.1748	0.1571	12.66	0.5690	58.02	5.86	101.48
Dark	Prx	c		56	0.0004	27.30	0.2343	0.1220	0.1613	13.97	0.4027	55.47	0.57	98.23
Dark	Prx	r		57	0.0005	25.71	0.4107	0.1341	0.0005	14.70	0.7734	55.86	3.36	100.95
Dark	Prx	c		58	0.0005	22.44	0.7562	0.2169	0.0050	12.58	0.5042	57.02	6.71	100.22
Dark	Prx	c		59	0.0005	25.31	0.2793	0.3321	0.2004	12.69	0.4180	54.47	5.12	98.82
Dark	Prx	r		60	0.0005	23.85	0.4868	0.6288	0.0006	15.76	0.9765	54.18	4.80	100.68
Dark	Prx	c	25	61	0.0006	24.63	0.0628	1.2159	0.0006	17.32	0.6972	54.45	2.33	100.70
Dark	Prx	r	25	62	0.0005	22.67	0.1786	1.5059	0.4380	19.90	0.8229	51.94	1.50	98.96
Dark	Prx	c	22.29	63	0.0006	23.67	0.0289	1.5552	0.0513	17.72	0.3710	56.04	1.83	101.26
Dark	Prx	r	22.29	64	0.0006	21.17	0.3650	1.5468	0.2578	18.68	0.5853	54.49	1.47	98.57
Dark	Prx	c	24.8	65	0.0006	24.70	0.0546	1.5491	0.1108	17.27	0.5399	54.43	1.36	100.01
Dark	Prx	r	24.8	66	0.0006	23.71	0.2791	1.6048	0.2726	16.24	0.4454	56.83	2.11	101.49
Dark	Prx	c	148.2	67	0.0007	21.72	0.0003	1.3782	0.1644	20.08	1.2935	54.59	0.83	100.05
Dark	Prx	r	148.2	68	0.0007	19.34	0.0252	0.7868	0.1501	23.38	1.5739	53.87	0.35	99.47
Dark	Prx	c	17.83	69	0.0006	28.76	0.0003	1.2121	0.0005	9.45	0.0007	59.24	2.03	100.70
Dark	Prx	r	17.83	70	0.0006	26.08	0.2752	2.1137	0.4067	12.59	0.1683	55.11	2.18	98.93

Supplementary Table 2C. Mineral analysis of dark and light bands (quartz).

Def.	Mineral	Analysis loc.	Size	Analysis id	Na ₂ O	MgO	K ₂ O	CaO	TiO ₂	FeO _t	MnO	SiO ₂	Al ₂ O ₃	Total
Dark	Q	c	170	3	0.0035	0.0029	0.36	0.003	0.004	0.006	0.302	96.90	0.003	97.58
Dark	Q	c	170	4	0.0036	0.0029	0.39	0.273	0.413	0.005	0.005	97.23	0.003	98.32
Dark	Q	c	70.37	5	0.0037	0.0030	0.28	0.054	0.082	0.005	0.005	102.74	0.003	103.18
Dark	Q	c	70.37	6	0.0036	0.0029	0.34	0.042	0.023	0.006	0.023	98.28	0.003	98.73
Dark	Q	c	112.5	7	0.0037	0.0030	0.40	0.003	0.004	0.005	0.005	102.53	0.003	102.95
Dark	Q	c	112.5	8	0.0036	0.0029	0.45	0.073	0.098	0.005	0.005	98.13	0.003	98.76
Dark	Q	c		33	0.0004	0.0003	0.75	0.000	0.001	0.271	0.001	95.12	0.000	96.14
Light	Q	c	412.9	47	0.0004	0.0003	0.79	0.123	0.301	0.274	0.130	97.32	0.000	98.94
Light	Q	c		48	0.0369	0.0004	3.72	0.088	0.001	0.613	0.001	88.29	7.216	99.96

Supplementary Table 2D. Mineral analysis of dark and light bands (Fe-Ti oxides).

Def.	Mineral	Analysis loc.	Size	Analysis id	Na ₂ O	MgO	K ₂ O	CaO	TiO ₂	FeO _t	MnO	SiO ₂	Al ₂ O ₃	Total
Dark	Mag	c		79	0.0014	1.5210	0.22	0.40	15.52	70.40	0.0008	2.73	3.37	94.16
Dark	Mag	c		80	0.0015	0.0010	0.14	0.20	0.13	91.95	0.0007	1.19	0.05	93.66



Supplementary Figure. CTAn software workflow for quantitative analysis of 3D images acquired from X-ray computed tomography.